Search for direct top squark pair production in final states with two leptons in $\sqrt{s}$ = 13 TeV pp collisions with the ATLAS detector

The ATLAS Collaboration

Abstract

The results of a search for direct pair production of top-squarks in events with two leptons (electrons or muons) are reported. The search uses 36.1 fb^{-1} of integrated luminosity from LHC pp collisions at $\sqrt{s}$ = 13 TeV collected by the ATLAS detector. To cover a range of mass differences between the top squark $\tilde{t}$ and lighter supersymmetric particles, four possible decay modes of the top squark are targeted with dedicated selections: the decay $\tilde{t} \rightarrow b\tilde{\chi}_1^{\pm}$ into a b-quark and the lightest chargino, the decay $\tilde{t} \rightarrow t\tilde{\chi}_1^0$ into an on-shell top quark and the lightest neutralino, the three-body decay $\tilde{t} \rightarrow bW\tilde{\chi}_1^0$ and the four-body decay $\tilde{t} \rightarrow b\ell\nu\tilde{\chi}_1^0$. No significant excess of events is observed above the Standard Model background for any selection, and cross-section limits are interpreted in limits on the $\tilde{t}$ and $\tilde{\chi}_1^0$ masses, significantly extending previous results.

1 Introduction

The Standard Model (SM) of particle physics is extremely successful in describing the phenomena of elementary particles and their interactions. Nevertheless it is believed to be a low energy realisation of a more general theory, because of the problems, inside the SM, related to the stabilisation of the Higgs mass against radiative corrections from Planck scale physics and of the need to explain the nature of dark matter (DM) [1–4]. Both shortcomings could be explained by new physics appearing at the TeV scale. This typically predicts new particles, motivating extensive searches at the LHC.

One of the most compelling theories beyond the SM is Supersymmetry (SUSY) [5–10]. SUSY is a spacetime symmetry that for each SM particle postulates the existence of a partner particle whose spin differs by one-half unit. The introduction of gauge-invariant and renormalisable interactions into SUSY models can violate the conservation of baryon number (B) and lepton number (L), resulting in a proton lifetime shorter than current experimental limits [11]. This is usually solved by assuming that the multiplicative quantum number R-parity [12], defined as $R = (-1)^{3(B-L)+2S}$, is conserved.

In the framework of a generic R-parity-conserving Minimal Supersymmetric Standard Model (MSSM) [13, 14], SUSY particles are produced in pairs, and the lightest supersymmetric particle (LSP) is stable and a candidate for dark matter [15, 16]. The scalar partners of right-handed and left-handed quarks (squarks), $\tilde{q}_R$ and $\tilde{q}_L$, can mix to form two mass eigenstates, $\tilde{q}_1$ and $\tilde{q}_2$, with $\tilde{q}_1$ defined to be the lighter one. In the case of the supersymmetric partner of the top quark, $\tilde{t}$, large mixing effects can lead to one top squark mass eigenstate, $\tilde{t}_1$, that is significantly lighter than the other squarks. The charginos and neutralinos are mixtures of the bino, winos and Higgsinos that are superpartners of the U(1) and SU(2) gauge bosons and the Higgs bosons, respectively. Their mass eigenstates are referred to as $\tilde{\chi}_i^\pm$ ($i = 1, 2$) and $\tilde{\chi}_j^0$ ($j = 1, 2, 3, 4$) in order of increasing masses. In a large variety of models, the LSP is the lightest neutralino $\tilde{\chi}_1^0$.

In this note a search for direct pair production of the top squark is reported, in final states with two isolated leptons (electrons or muons) and missing transverse momentum. The search utilizes 36.1 fb^{-1}of proton-proton collision data collected by the ATLAS experiment in 2015 and 2016 at a centre-of-mass energy $\sqrt{s} = 13$ TeV.

The top squark is assumed to decay to either the lightest chargino or the lightest neutralino. Depending on the mass difference between the top squark and the lighter SUSY particles different decay modes are relevant. The decays $\tilde{t} \rightarrow t\tilde{\chi}_1^0$ and $\tilde{t} \rightarrow b\tilde{\chi}_1^\pm$ dominate when they are kinematically accessible. For intermediate mass differences, $m_{\tilde{\chi}_1^0} + m_W + m_b < m_{\tilde{t}} < m_{\tilde{\chi}_1^0} + m_t$, the three body decay $\tilde{t} \rightarrow bW\tilde{\chi}_1^0$ is considered. For smaller mass differences, the four body decay channel $\tilde{t} \rightarrow bff'\tilde{\chi}_1^0$, where f and f' are two fermions from the W^* decay, is assumed to occur. In this search, f and f' are a lepton and its associated neutrino. For each of these decay modes, shown by the diagrams in Figure 1, a dedicated event selection is performed to optimize the search significance, as detailed in Table 1.

The results of the searches are interpreted in simplified models [17–19] as a function of the top squark and lightest neutralino masses. Additionally, results are also interpreted in one pMSSM [20, 21] model
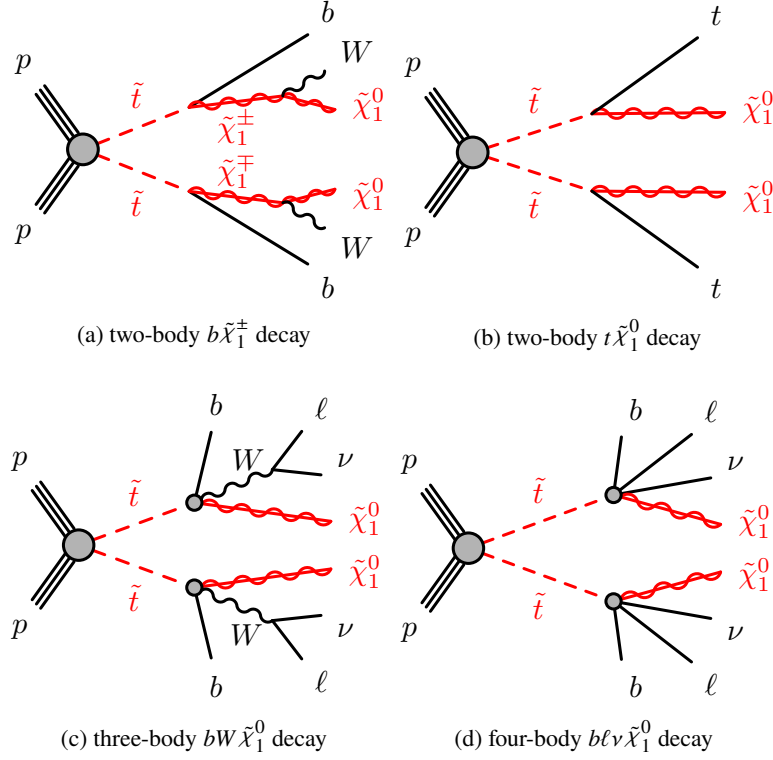
Figure 1: Diagrams representing the four main signals targeted by the analyses: (a) the decay of the top squark via the lightest chargino ($\tilde{t} \to b\tilde{\chi}_1^\pm$), (b) the 2-body decay into an on-shell top quark and the lightest neutralino ($\tilde{t} \to t\tilde{\chi}_1^0$), (c) the 3-body decay mode into an on-shell W boson, a b quark and the lightest neutralino ($\tilde{t} \to bW\tilde{\chi}_1^0$) and (d) the 4-body decay mode ($\tilde{t} \to bff'\tilde{\chi}_1^0$) where the two fermions f and f' are a lepton with its neutrino in this article.

including the following decay modes: $\tilde{t} \to t\tilde{\chi}_1^0$, $\tilde{t} \to b\tilde{\chi}_1^\pm$ with $\tilde{\chi}_1^\pm \to W\tilde{\chi}_1^0$ and $\tilde{t} \to t\tilde{\chi}_2^0$, with $\tilde{\chi}_2^0 \to h/Z\tilde{\chi}_1^0$. Previous ATLAS [22, 23] and CMS [24–36] analyses have set exclusion limits at 95% confidence level (CL) on the signal scenarios considered here. When considering simplified models including the $\tilde{t} \to t\tilde{\chi}_1^0$ decay, top squark masses up to about 700 GeV have been excluded for a nearly massless lightest neutralino. For the same assumptions on the lightest neutralino mass, if the $\tilde{t} \to b\tilde{\chi}_1^\pm$ decay is considered, top squark masses up to about 500 GeV have been excluded.

Table 1: Summary of the sections dedicated to the two-body, three-body and four-body selections and signal types targeted by each selection.

	two-body	three-body	four-body
Variables	Section 4.1		
Event selection	Section 4.2	Section 4.3	Section 4.4
Background determination	Section 6.1	Section 6.2	Section 6.3
Results	Section 8.1	Section 8.2	Section 8.3
Interpretation	Section 8.4		
Targeted decay modes	$b\tilde{\chi}_1^\pm$ and $t\tilde{\chi}_1^0$	$bW\tilde{\chi}_1^0$	$b\ell\nu\tilde{\chi}_1^0$
Signal diagram	Figure 1(a) and 1(b)	Figure 1(c)	Figure 1(d)
Targeted $m_{\tilde{t}}$ range	$> m_b + m_{\tilde{\chi}_1^\pm}$	$\geq m_b + m_W + m_{\tilde{\chi}_1^0}$	$< m_b + m_W + m_{\tilde{\chi}_1^0}$
	or $> m_t + m_{\tilde{\chi}_1^0}$	and $< m_t + m_{\tilde{\chi}_1^0}$	

2 ATLAS detector

The ATLAS detector [37] at the LHC is a multi-purpose particle detector with a cylindrical forward-backward symmetric geometry[1] and an approximate 4π coverage in solid angle. It consists of an inner tracking detector (ID) surrounded by a thin superconducting solenoid providing a 2 T axial magnetic field, electromagnetic and hadron calorimeters, and a muon spectrometer. The inner tracking detector covers the pseudorapidity range $|\eta| < 2.5$. It consists of silicon pixel, silicon micro-strip, and transition radiation tracking detectors. The newly installed innermost layer of pixel sensors [38] was operational for the first time during the 2015 data taking. Lead/liquid-argon (LAr) sampling calorimeters provide electromagnetic (EM) energy measurements with high granularity. A hadron (steel/scintillator-tile) calorimeter covers the central pseudorapidity range ($|\eta| < 1.7$). The end-cap and forward regions are instrumented with LAr calorimeters for both EM and hadronic energy measurements up to $|\eta| = 4.9$. The muon spectrometer surrounds the calorimeters and is based on three large air-core toroid superconducting magnets with eight coils each. It includes a system of precision tracking chambers and fast detectors for triggering. The average toroid field strength is approximately 0.5 T in the central region and 1 T in the end-cap regions.

3 Data samples and event reconstruction

The data were collected by the ATLAS detector in 2015 and 2016 during pp collisions at a centre-of-mass energy of $\sqrt{s} = 13$ TeV, with a peak instantaneous luminosity of $\mathcal{L} = 1.4 \times 10^{34}$ cm^{-2}s^{-1}, a bunch spacing

---

[1] ATLAS uses a right-handed coordinate system with its origin at the nominal interaction point (IP) in the centre of the detector and the z-axis along the beam pipe. The x-axis points from the IP to the centre of the LHC ring, and the y-axis points upwards. Cylindrical coordinates (r, ϕ) are used in the transverse plane, ϕ being the azimuthal angle around the z-axis. The pseudorapidity is defined in terms of the polar angle θ as $\eta = -\ln\tan(\theta/2)$.

of 25 ns, and an average number of pp interactions per bunch crossing (pile-up) of $\langle\mu\rangle = 14$ in 2015 and $\langle\mu\rangle = 24$ in 2016. Only events taken in stable beam conditions, and for which all relevant detector systems were operational, are considered in this analysis. After data-quality requirements, the data sample amounts to an integrated luminosity of 36.1 fb^{-1} with an uncertainty of ±3.2%. This uncertainty is derived, following a methodology similar to that detailed in Ref. [39], from a preliminary calibration of the luminosity scale using $x - y$ beam-separation scans performed in August 2015 and May 2016.

Candidate events are required to have a reconstructed vertex with at least two associated tracks with transverse momentum $p_T > 400$ MeV. The vertex with the highest scalar sum of the squared transverse momenta of the associated tracks is considered the primary vertex of the event.

Electron (*baseline*) candidates are reconstructed from three-dimensional electromagnetic calorimeter energy depositions matched to ID tracks, and are required to have pseudorapidity $|\eta| < 2.47$, $p_T > 7$ GeV, and to pass a loose likelihood-based identification requirement [40]. The likelihood input variables include measurements of calorimeter shower shapes and of track properties from the ID.

Muon (*baseline*) candidates are reconstructed in the pseudorapidity region $|\eta| < 2.4$ from muon spectrometer tracks matching ID tracks. They must have $p_T > 7$ GeV and must pass the medium identification requirements defined in Ref. [41], based on requirements on the number of hits in the different ID and muon spectrometer subsystems, and on the significance of the charge to momentum ratio (q/p) measurement [41].

Jets are reconstructed from three-dimensional energy clusters in the calorimeter [42] with the anti-k_t jet clustering algorithm [43] with a radius parameter $R = 0.4$. Only jet candidates with $p_T > 20$ GeV and $|\eta| < 2.8$ are considered. Jets are calibrated as described in Refs. [44, 45], and the expected average energy contribution from pile-up clusters is subtracted according to the jet area [46]. Additional selections are applied on jets with $p_T < 60$ GeV and $|\eta| < 2.4$ in order to reject jets produced in pile-up collisions [47]. The "medium" working point is used for the pile-up rejection, which has an efficiency of about 92% for jets produced by the hard scatter. Jets resulting from the hadronisation of b-quarks are identified using the multivariate MV2c10 b-tagging algorithm, which is based on quantities such as impact parameters of associated tracks and reconstructed secondary vertices [48, 49]. This algorithm is used at a working point that provides 77% b-tagging efficiency in simulated $t\bar{t}$ events, and a rejection factor of 134 for light-quark flavours and gluons and 6 for charm jets. The jets satisfying the b-tagging requirements are referred to as b-jets.

Events are discarded if they contain any jet with $p_T > 20$ GeV failing basic quality selection criteria that reject detector noise and non-collision backgrounds [50].

To resolve reconstruction ambiguities, an overlap removal algorithm is applied on candidate leptons and jets. Non-b-tagged jets which are at $\Delta R = \sqrt{(\Delta y)^2 + (\Delta \phi)^2} < 0.2$ (here y stands for the rapidity) from an electron candidate are removed, and the same is done for jets which lie close to a muon candidate and are consistent with the characteristics of jets produced by muon bremsstrahlung. Finally, any lepton candidate within $\Delta R < 0.4$ from the direction of a surviving jet candidate is removed, in order to reject

leptons from the decay of a b or c hadron. Electrons which share an ID track with a muon candidate are also removed.

Additional selections are then applied to the remaining lepton and jet candidates. Tighter requirements on the lepton candidates are imposed, which are then referred to as "signal" electrons or muons. Signal electrons must satisfy the *medium* likelihood-based identification requirement as defined in Ref. [40]. Signal electrons must have a significance of the transverse impact parameter with respect to the reconstructed primary vertex, d_0, of $|d_0|/\sigma(d_0) < 5$. For signal muons, the corresponding requirement is $|d_0|/\sigma(d_0) < 3$. The tracks associated to the signal leptons must have a longitudinal impact parameter with respect to the reconstructed primary vertex, z_0, satisfying $|z_0 \sin \theta| < 0.5$ mm. Leptons are required to be isolated from other activity using a relatively loose criterion designed to be satisfied by 99% of leptons from Z decays. Jets are required to have $|\eta| < 2.5$.

The missing transverse momentum (E_T^{miss}) is defined as the magnitude of the two-vector $\mathbf{p}_T^{miss}$ which is the negative vector sum of the transverse momenta of all identified baseline physics objects (electrons, muons, jets) and an additional soft term. The soft term is constructed from all tracks that are not associated with any physics object, but which are associated with the primary vertex. In this way, the E_T^{miss} is adjusted for the best calibration of the jets and the other identified physics objects above, while maintaining pile-up independence in the soft term [51, 52].

4 Event selection

For the two-body and three-body selections, events are accepted if they pass an online selection (trigger) requiring a minimum of two electrons, two muons or an electron and a muon matched to the trigger objects. The offline selection requires that the leading lepton has a p_T larger than 25 GeV and the subleading lepton a p_T larger than 20 GeV, ensuring that trigger efficiencies are constant in the relevant phase space. The four-body selection accepts events passing an E_T^{miss}-based trigger and having offline $E_T^{miss} > 200$ GeV. Using this trigger permits the use of a reduced lepton p_T threshold of 7 GeV, increasing acceptance for the low lepton p_T produced in the four-body $\tilde{t} \rightarrow b\ell\nu\tilde{\chi}_1^0$ decay.

Events are required to have exactly two signal leptons which must be of opposite charge (electrons, muons, or one of each) with an invariant mass (regardless of the flavours of the leptons in the pair) $m_{\ell\ell}$ greater than 20 GeV (10 GeV in case of four-body selection) in order to remove leptons from low mass resonances. Except for the four-body selection, events with same flavour (SF) lepton pairs between 71.2 and 111.2 GeV are rejected, in order to reduce the backgrounds with leptons produced by Z bosons. No additional selection is applied on the $m_{\ell\ell}$ of different flavour (DF) lepton pairs. In the following, the requirements described in the preceding part of this section will be referred to as "common selection".

4.1 Discriminators and kinematic variables

For the different decay modes considered, dedicated sets of discriminating variables are used to separate the signal from the SM backgrounds.

The missing transverse momentum and the p_{T} of the leading leptons and jets are used to define three useful ratio variables :

$$R_1 = E_{\mathrm{T}}^{\mathrm{miss}}/(E_{\mathrm{T}}^{\mathrm{miss}} + p_{\mathrm{T}}(\ell_1) + p_{\mathrm{T}}(\ell_2) + p_{\mathrm{T}}(j_1) + p_{\mathrm{T}}(j_2)), \tag{1}$$

$$R_{\ell\ell} = E_{\mathrm{T}}^{\mathrm{miss}}/(p_{\mathrm{T}}(\ell_1) + p_{\mathrm{T}}(\ell_2)), \tag{2}$$

and

$$R_{\ell j} = E_{\mathrm{T}}^{\mathrm{miss}}/(E_{\mathrm{T}}^{\mathrm{miss}} + p_{\mathrm{T}}(\ell_1) + p_{\mathrm{T}}(\ell_2) + \sum_{i=1,\ldots,N \leq 4} p_{\mathrm{T}}(j_i)), \tag{3}$$

where $p_{\mathrm{T}}(\ell_1)$ and $p_{\mathrm{T}}(\ell_2)$ are the leading and subleading lepton transverse momenta respectively and $p_{\mathrm{T}}(j_{i=1,\ldots,N \leq 4})$ are the transverse momenta in decreasing order of up to the four leading jets. R_1 and $R_{\ell\ell}$ are used to reject backgrounds, e.g. Z/γ^* + jets, which peak at lower values than the signal. Similarly, $R_{\ell j}$ is a powerful discriminant against multi-jet events.

Other variables employed are :

- $\mathbf{p}_{\mathrm{T,boost}}^{\ell\ell}$: defined as the vector

$$\mathbf{p}_{\mathrm{T,boost}}^{\ell\ell} = \mathbf{p}_{\mathrm{T}}^{\mathrm{miss}} + \mathbf{p}_{\mathrm{T}}(\ell_1) + \mathbf{p}_{\mathrm{T}}(\ell_2). \tag{4}$$

  The $\mathbf{p}_{\mathrm{T,boost}}^{\ell\ell}$ variable, with magnitude $p_{\mathrm{T,boost}}^{\ell\ell}$, can be interpreted as the opposite of the vector sum of all the transverse hadronic activity in the event.

- $\Delta\phi_{\mathrm{boost}}$: the azimuthal angle between the $\mathbf{p}_{\mathrm{T}}^{\mathrm{miss}}$ vector and the $\mathbf{p}_{\mathrm{T,boost}}^{\ell\ell}$ vector.

- Δx: defined as

$$\Delta x = \frac{2 \cdot (p_{\mathrm{z}}(\ell_1) + p_{\mathrm{z}}(\ell_2))}{E_{\mathrm{CM}}} \tag{5}$$

  where $E_{\mathrm{CM}} = 13$ TeV is used and $p_{\mathrm{z}}(\ell_1), p_{\mathrm{z}}(\ell_2)$ are respectively the leading and subleading lepton longitudinal momenta. This variable helps to discriminate between gluon and quark-initiated processes. The former tend to peak towards zero, while the latter tend to peak at higher values.

- $\cos\theta_b$: the cosine of the angle between the direction of motion of either of the two leptons and the beam axis in the centre-of-mass frame of the two leptons [53]. This variable is sensitive to the spin of the pair-produced particle, providing additional rejection against diboson backgrounds.

- $m_{\mathrm{T2}}^{\ell\ell}$: lepton-based stransverse mass. The stransverse mass defined in [54, 55] is a kinematic variable used to bound the masses of a pair of particles which have each decayed to a visible and an

invisible particle. This quantity is defined as

$$m_{\text{T2}}(\mathbf{p}_{\text{T},1}, \mathbf{p}_{\text{T},2}, \mathbf{q}_{\text{T}}) = \min_{\mathbf{q}_{\text{T},1}+\mathbf{q}_{\text{T},2}=\mathbf{q}_{\text{T}}} \{ \max[\, m_{\text{T}}(\mathbf{p}_{\text{T},1}, \mathbf{q}_{\text{T},1}), m_{\text{T}}(\mathbf{p}_{\text{T},2}, \mathbf{q}_{\text{T},2})\,]\}, \tag{6}$$

where m_{T} indicates the transverse mass,[2] $\mathbf{p}_{\text{T},1}$ and $\mathbf{p}_{\text{T},2}$ are the transverse momentum vectors of two particles, and $\mathbf{q}_{\text{T},1}$ and $\mathbf{q}_{\text{T},2}$ are vectors with $\mathbf{q}_{\text{T}} = \mathbf{q}_{\text{T},1} + \mathbf{q}_{\text{T},2}$. The minimisation is performed over all the possible decompositions of $\mathbf{q}_{\text{T}}$. For $t\bar{t}$ or WW decays, when the transverse momenta of the two leptons in each event are taken as $\mathbf{p}_{\text{T},1}$ and $\mathbf{p}_{\text{T},2}$, and $\mathbf{p}_{\text{T}}^{\text{miss}}$ as $\mathbf{q}_{\text{T}}$, $m_{\text{T2}}(\mathbf{p}_{\text{T}}(\ell_1), \mathbf{p}_{\text{T}}(\ell_2), \mathbf{p}_{\text{T}}^{\text{miss}})$ is bounded sharply from above by the mass of the W boson [56, 57]. In the $\tilde{t}_1 \rightarrow b\tilde{\chi}_1^\pm$ decay mode the upper bound is strongly correlated with the mass difference between the chargino and the lightest neutralino. In this paper, $m_{\text{T2}}(\mathbf{p}_{\text{T}}(\ell_1), \mathbf{p}_{\text{T}}(\ell_2), \mathbf{p}_{\text{T}}^{\text{miss}})$ is referred to simply as $m_{\text{T2}}^{\ell\ell}$.

The three-body selection uses a number of "super-razor" variables that are defined in Ref. [58]. They are designed to identify events with two massive parent particles (i.e. top squarks) that each decay into a set of visible (only leptons are considered in this case, all other particles including jets are ignored) and invisible particles (i.e. neutrinos and neutralinos). These variables are:

- $R_{p_{\text{T}}}$: The quantity $R_{p_{\text{T}}}$ is defined as:

$$R_{p_{\text{T}}} = \frac{|\vec{J}_{\text{T}}|}{|\vec{J}_{\text{T}}| + \sqrt{\hat{s}_{\text{R}}}/4}, \tag{7}$$

where $\vec{J}_{\text{T}}$ is the vector sum of the transverse momenta of the visible particles and the missing transverse momentum, and $\sqrt{\hat{s}_{\text{R}}}$ is a measure of the system's energy in the razor frame R as defined in Ref. [58] as the frame in which the two visible leptons have equal and opposite p_{z}. In the case where all possible visible particles are considered, the razor frame R becomes an approximation of the pair production centre-of-mass frame with the centre-of-mass energy $\sqrt{\hat{s}_{\text{R}}}$. In this analysis only leptons are considered in the visible system. Therefore, $R_{p_{\text{T}}}$ will tend towards zero in events that do not contain additional activity (i.e. dibosons) due to vanishing $|\vec{J}_{\text{T}}|$, whereas in events that contain additional activity (i.e. $t\bar{t}$) this variable will tend towards unity, thus providing separation power between the two cases.

- $\gamma_{\text{R}+1}$: The Lorentz factor associated with the boosts from the razor frame R to the approximations of the two decay frames of the parent particles. It is a measure of how the two visible systems are distributed, tending towards unity when the visible particles are back-to-back or having different momenta, while preferring lower values when they are equal in momenta and collinear.

- M_Δ^{R}: The quantity M_Δ^{R} is defined as:

$$M_\Delta^{\text{R}} = \frac{\sqrt{\hat{s}_{\text{R}}}}{\gamma_{\text{R}+1}}. \tag{8}$$

---

[2] The transverse mass is defined by the equation $m_{\text{T}}(\mathbf{p}_{\text{T}}, \mathbf{q}_{\text{T}}) = \sqrt{2|\mathbf{p}_{\text{T}}||\mathbf{q}_{\text{T}}|(1 - \cos(\Delta\phi))}$, where $\Delta\phi$ is the angle between the particles of negligible mass with transverse momenta $\mathbf{p}_{\text{T}}$ and $\mathbf{q}_{\text{T}}$.

This variable has a kinematic end-point that is proportional to the mass-splitting between the parent particle and the invisible particle. Therefore, it provides rejection against both top-quark and diboson production processes when it is required to be greater than the mass of the W boson, and in this case it also helps to reject the residual Z/γ^* + jets background.

- $\Delta\phi_\beta^{\mathrm{R}}$: The quantity $\Delta\phi_\beta^{\mathrm{R}}$ is the azimuthal angle between the razor boost from the laboratory to the R frame and the sum of the visible momenta as evaluated in the R frame. For systems where the invisible particle has a mass that is comparable to the pair-produced massive particle, this variable has a pronounced peak near π, making it, in general, a good discriminator in searches for models with small mass differences.

4.2 Two-body event selection

This selection targets the top squark two-body decays (Figures 1(a),1(b)) to either a bottom quark and a chargino, with the chargino decaying into the lightest neutralino and a W boson, or a near-mass-shell top quark and a neutralino.

In these decays, the kinematic properties of signal events are similar to those of $t\bar{t}$ events. In particular, when the top squarks are produced at rest the momenta carried by the neutralinos in the final state are small and the discrimination difficult. A better separation between signal events and the $t\bar{t}$ background can be obtained for top squark pairs which recoil from initial state radiation (ISR).

Three signal regions (SRs), summarised in Table 2 and denoted as $\mathrm{SR(A,B,C)}_x^{2-\mathrm{body}}$, where x stands for the lower bound of the $m_{\mathrm{T2}}^{\ell\ell}$ interval, have been optimised to target different scenarios:

- $\mathrm{SRA}_{180}^{2-\mathrm{body}}$ targets the decays to $b\tilde{\chi}_1^\pm$ in scenarios where $m_{\tilde{t}_1} - m_{\tilde{\chi}_1^\pm}$ is below 10 GeV and the b-jets from the decay of the $\tilde{t}_1$ are too low-energy to be reconstructed. For this reason, b-jets with $p_{\mathrm{T}} > 25$ GeV are vetoed to reduce the contamination from SM processes including top quarks. No further requirement is applied on the hadronic activity of the event. Events with SF leptons are required to have $m_{\ell\ell} > 111.2$ GeV and $R_1 > 0.3$ to reduce the contamination from Z/γ^* + jets events. The contribution from diboson production is expected to be the dominant background in the SR and it is reduced by requiring the events to have $\Delta x < 0.07$. Furthermore, events are required to have $m_{\mathrm{T2}}^{\ell\ell} > 180$ GeV.

- $\mathrm{SRB}_{140}^{2-\mathrm{body}}$ targets the decays to $b\tilde{\chi}_1^\pm$ in scenarios with a mass splitting between the top squark and the chargino larger than 10 GeV, such that the jets from the hadronisation of b quarks are expected to be detectable. At least two jets with $p_{\mathrm{T}} > 25$ GeV are required, with at least one of them being identified as a b-jet. Events from $t\bar{t}$ and Z/γ^* + jets production are suppressed by requiring $\Delta\phi_{\mathrm{boost}} < 1.5$. The main expected SM processes satisfying this selection are $t\bar{t}$ and $t\bar{t}$ +Z with the Z boson decaying to neutrinos. A final selection of $m_{\mathrm{T2}}^{\ell\ell} > 140$ GeV is applied. Because of the similar final state, this selection has also been found to be the most sensitive to signal scenarios in which the $\tilde{t}_1$ decays to $t + \tilde{\chi}_1^0$, with large $m_{\tilde{t}_1} - m_{\tilde{\chi}_1^0}$.

- $\mathrm{SRC}^{2-\mathrm{body}}_{110}$ targets the decays to $t + \tilde{\chi}^0_1$, in scenarios where $m_{\tilde{t}_1} \sim m_{\tilde{\chi}^0_1} + m_t$. Candidate events are required to have $E^{\mathrm{miss}}_{\mathrm{T}} > 200$ GeV and at least three jets with $p_{\mathrm{T}} > 25$ GeV, where one of the jets is interpreted as ISR. The other two jets are expected to arise from the decay of the top quarks in the final state. One of the jets in the event is required to be b-tagged, effectively separating the signal events from SM diboson production. The $Z/\gamma^* +$ jets background is suppressed by requiring $R_{\ell\ell}$ to be larger than 1.2. Events are finally required to have $m^{\ell\ell}_{\mathrm{T2}} > 110$ GeV.

For the model-dependent exclusion limits, a shape fit of the $m^{\ell\ell}_{\mathrm{T2}}$ distribution is performed in the $\mathrm{SRA}^{2-\mathrm{body}}_{180}$ and $\mathrm{SRB}^{2-\mathrm{body}}_{140}$ selections: the distribution is divided in bins of width 20 GeV, starting from $m^{\ell\ell}_{\mathrm{T2}} = 120$ GeV; the last bin low boundary corresponds to the requirement on the same variable in the definitions of $\mathrm{SRA}^{2-\mathrm{body}}_{180}$ and $\mathrm{SRB}^{2-\mathrm{body}}_{140}$; each bin is referred to as $\mathrm{SR(A, B)}^{2-\mathrm{body}}_{\mathrm{x,y}}$, where x and y denote the low and high edges of the bin.

Table 2: *Two-body selection* signal region definitions.

	$\mathrm{SRA}^{2-\mathrm{body}}_{180}$		$\mathrm{SRB}^{2-\mathrm{body}}_{140}$		$\mathrm{SRC}^{2-\mathrm{body}}_{110}$	
Lepton flavour	SF	DF	SF	DF	SF	DF
$p_{\mathrm{T}}(\ell_1), p_{\mathrm{T}}(\ell_2)$ [GeV]	> 25, > 20		> 25, > 20		> 25, > 20	
$m_{\ell\ell}$ [GeV]	> 111.2	> 20	[20,71.2] or > 111.2	> 20	[20,71.2] or > 111.2	> 20
R_1	> 0.3	–	–		–	
$R_{\ell\ell}$	–		–		> 1.2	
Δx	< 0.07		–		–	
$\Delta\phi_{\mathrm{boost}}$	–		< 1.5		–	
n_{jets}	–		≥ 2		≥ 3	
$n_{b-\mathrm{jets}}$	= 0		≥ 1		≥ 1	
$E^{\mathrm{miss}}_{\mathrm{T}}$ [GeV]	–		–		> 200	
$m^{\ell\ell}_{\mathrm{T2}}$ [GeV]	> 180		> 140		> 110	

4.3 Three-body event selection

This selection targets the top squark three-body decay mode (Figure 1(c)), which is expected to be the dominant decay mode when the two-body decay mode into the lightest chargino or neutralino is kinematically forbidden, i.e. for $m_{\tilde{\chi}^0_1} + m_W + m_b < m_{\tilde{t}_1} < m_{\tilde{\chi}^\pm_1} + m_b$ and $m_{\tilde{t}_1} < m_{\tilde{\chi}^0_1} + m_t$.

Two orthogonal signal regions, $\mathrm{SR}^{3-\mathrm{body}}_W$ and $\mathrm{SR}^{3-\mathrm{body}}_t$, are summarised in Table 3. $\mathrm{SR}^{3-\mathrm{body}}_W$ targets the region where $\Delta m(\tilde{t}, \tilde{\chi}^0_1) \sim m_W$ in which the produced b-jets have low transverse momentum, and hence are often not reconstructed. The second signal region $\mathrm{SR}^{3-\mathrm{body}}_t$ targets the region in which $\Delta m(\tilde{t}, \tilde{\chi}^0_1) \sim m_t$.

Both regions make use of a common set of requirements on R_{p_T}, $\gamma_{\mathrm{R}+1}$, and in the two-dimensional ($\cos\theta_b$, $\Delta\phi^\mathrm{R}_\beta$) plane. In addition, $\mathrm{SR}^{3-\mathrm{body}}_W$ requires that no b-jet is identified in the event and that $M^\mathrm{R}_\Delta > 95$ GeV.

The large M_Δ^R requirement suppresses the top quark and diboson backgrounds. In the case of SR_t^{3-body}, the requirements are: at least one b-jet and $M_\Delta^R > 110$ GeV. The b-jet requirement makes the selection orthogonal to SR_W^{3-body}, so that the two SRs can be statistically combined. Furthermore a slightly tighter M_Δ^R requirement is necessary to eliminate the background that originates from top-quark production processes.

Table 3: *Three-body selection* signal region definitions.

	SR_W^{3-body}		SR_t^{3-body}	
Lepton flavour	SF	DF	SF	DF
$p_T(\ell_1), p_T(\ell_2)$ [GeV]	$> 25, > 20$		$> 25, > 20$	
$m_{\ell\ell}$ [GeV]	[20,71.2] or > 111.2	> 20	[20,71.2] or > 111.2	> 20
n_{b-jets}	$= 0$		≥ 1	
M_Δ^R [GeV]	> 95		> 110	
R_{p_T}	> 0.7		> 0.7	
$1/\gamma_{R+1}$	> 0.7		> 0.7	
$\Delta\phi_\beta^R$	$> 0.9|\cos\theta_b| + 1.6$		$> 0.9|\cos\theta_b| + 1.6$	

4.4 Four-body event selection

The selection described here targets the four-body decay mode of the top squark (Figure 1(d)) for scenarios where $m_{\tilde{t}_1} < m_{\tilde{\chi}_1^0} + m_b + m_W$ and $m_{\tilde{t}_1} < m_{\tilde{\chi}_1^\pm} + m_b$. In this region the top squark decay into $c\tilde{\chi}_1^0$ might be dominant, depending on various SUSY model parameters. The branching fraction to this final state is here assumed to be negligible. For these small mass splittings, the leptons in the final state, originating from the virtual W boson decays, are expected to have low p_T.

Signal events can be distinguished from SM processes if a high-p_T jet from ISR leads to a large transverse boost of the sparticle pair system and enhances the E_T^{miss}. At least two jets with $p_T > 25$ GeV are required in the event. The leading jet is considered to be the ISR jet and required to have $p_T > 150$ GeV. Since the jets resulting from $\tilde{t}$ decays tend to have low p_T in this scenario, at most one more energetic jet with $p_T > 25$ GeV is permitted in the event and the transverse momentum of the third jet (if present) must satisfy $p_T(j_3)/E_T^{miss} < 0.14$.

In order to remove events originating from low-mass resonances, the invariant mass of the two leptons, $m_{\ell\ell}$, is required to be greater than 10 GeV. Furthermore, upper limits on $p_T(\ell_1)$ and $p_T(\ell_2)$, respectively of 80 GeV and 35 GeV, are applied.

The signal region SR^{4-body} is defined as summarised in Table 4. The two variables $R_{\ell j}$ and $R_{\ell\ell}$ must be larger than 0.35 and 12 to reject multi-jet and $t\bar{t}$ backgrounds, respectively. Finally, the two most energetic jets in the event must not be tagged as b-jets.

Table 4: *Four-body selection* signal region definition.

	SR$^{4-\text{body}}$
Lepton flavour	SF and DF
$E_{\text{T}}^{\text{miss}}$ [GeV]	> 200
$p_{\text{T}}(\ell_1)$ [GeV]	[7,80]
$p_{\text{T}}(\ell_2)$ [GeV]	[7,35]
$m_{\ell\ell}$ [GeV]	> 10
n_{jets}	≥ 2
$p_{\text{T}}(j_1)$ [GeV]	> 150
$p_{\text{T}}(j_2)$ [GeV]	> 25
$p_{\text{T}}(j_3)/E_{\text{T}}^{\text{miss}}$	< 0.14
$R_{\ell j}$	> 0.35
$R_{\ell\ell}$	> 12
$n_{b-\text{jets}}$	veto on j_1 and j_2

5 Samples of simulated events

Monte Carlo (MC) simulated event samples are used to aid in the estimation of the background from SM processes and to model the SUSY signal. The generator, parton shower and hadronisation generator, cross-section normalisation, parton distribution function (PDF) set and underlying-event tune of these samples are given in Table 5, and more details on the generator configurations can be found in Refs. [59–62]. Cross-sections calculated at next-to-next-to-leading order (NNLO) in QCD including resummation of next-to-next-to-leading logarithmic (NNLL) soft gluon terms are used for top-quark production processes. For production of top-quark pairs in association with vector or Higgs bosons, cross-sections calculated at next-to-leading order (NLO) are used, and the generator cross-sections calculated by SHERPA (at NLO for most of the processes) are used when normalising the multi-boson backgrounds. In all MC samples, except those produced by SHERPA, the EVTGEN v1.2.0 program [63] is used to model the properties of the bottom and charm hadron decays. Additional MC samples are used when calculating systematic uncertainties, as detailed in Section 7.

SUSY signal samples are generated from leading-order (LO) matrix elements with up to two extra partons, using the MADGRAPH5_AMC@NLO v2.2.3 generator. The two-body signals use PYTHIA 8.186 for the modelling of the SUSY decay chain, parton showering, hadronisation and the description of the underlying event. The three-body and four-body signals are decayed with PYTHIA8.2+MADSPIN [88] instead. Parton luminosities are provided by the NNPDF23LO PDF set. Jet–parton matching is realised following the CKKW-L prescription [89], with a matching scale set to one quarter of the pair-produced superpartner mass. In all cases, the mass of the top quark is fixed at 172.5 GeV. Signal cross-sections are calculated to next-to-leading order in the strong coupling constant, adding the resummation of soft gluon emission at next-to-leading-logarithmic accuracy (NLO+NLL) [70, 90, 91]. The nominal cross-sections and their uncertainties are taken from an envelope of cross-section predictions using different PDF sets and factorisation and renormalisation scales, as described in Ref. [71]. All two-, three- and four-body

Table 5: Simulated signal and background event samples: the corresponding generator, parton shower generator, cross-section normalisation, PDF set and underlying-event tune are shown.

Physics process	Generator	Parton shower generator	Cross-section normalisation	PDF set	Tune
SUSY Signals	MADGRAPH5_AMC@NLO 2.2.3 [64]	PYTHIA 8.186 [65]	NLO+NLL [66–71]	NNPDF2.3LO [72]	A14 [73]
Z/γ^* + jets	SHERPA 2.2.1 [74]	SHERPA 2.2.1	NNLO [75]	NLO CT10 [72]	SHERPA default
$t\bar{t}$	POWHEG-BOX v2 [76]	PYTHIA 6.428 [77]	NNLO+NNLL [78–83]	NLO CT10	PERUGIA2012 [84]
Wt	POWHEG-BOX v2	PYTHIA 6.428	NNLO+NNLL [85]	NLO CT10	PERUGIA2012
$t\bar{t}W/Z/\gamma^*$	MADGRAPH5_AMC@NLO 2.2.2	PYTHIA 8.186	NLO [64]	NNPDF2.3LO	A14
Diboson	SHERPA 2.2.1	SHERPA 2.2.1	Generator NLO	NLO CT10	SHERPA default
$t\bar{t}h$	MADGRAPH5_AMC@NLO 2.2.2	HERWIG 2.7.1 [86]	NLO [87]	CTEQ6L1	A14
Wh, Zh	MADGRAPH5_AMC@NLO 2.2.2	PYTHIA 8.186	NLO [87]	NNPDF2.3LO	A14
$t\bar{t}WW$, $t\bar{t}t\bar{t}$	MADGRAPH5_AMC@NLO 2.2.2	PYTHIA 8.186	NLO [64]	NNPDF2.3LO	A14
tZ, tWZ, $t\bar{t}t$	MADGRAPH5_AMC@NLO 2.2.2	PYTHIA 8.186	LO	NNPDF2.3LO	A14
Triboson	SHERPA 2.2.1	SHERPA 2.2.1	Generator LO, NLO	CT10	SHERPA default

samples are generated assuming a 100% branching ratio to the respective final states.

For the pMSSM inspired models, the mass spectrum of sparticles is calculated using SOFTSUSY 3.7.3 [92] and cross-checked with SPHENO 3.3.8 [93, 94] and SUSPECT 2.5 [95]. HDECAY and SDECAY, included in SUSY-HIT [96] are used to generate decay tables of the SUSY particles.

To simulate the effects of additional pp collisions in the same and nearby bunch crossings, additional interactions are generated using the soft QCD processes of PYTHIA 8.186 with the A2 tune [97] and the MSTW2008LO PDF set [98], and they are overlaid onto each simulated hard scatter event. The MC samples are reweighted to the pile-up distribution observed in the data. The MC samples are processed through an ATLAS detector simulation [99] based on GEANT4 [100] or, in the case of $t\bar{t}t$ and the SUSY signal samples, a fast simulation using a parameterisation of the calorimeter response and GEANT4 for the other parts of the detector [101]. All MC samples are reconstructed in the same manner as the data. Corrections derived from data control samples are applied to simulated events to account for differences between data and simulation in reconstruction efficiencies, momentum scale and resolution of leptons and in the efficiency and false positive rate for identifying b-jets.

6 Determination of Standard Model backgrounds

The dominant SM background processes satisfying the SR requirements are estimated by simulation, which is normalised and verified in separate regions of the phase space. Dedicated control regions (CRs), described in Sections 6.1-6.3, enhanced in a particular background component are used for the normalisation. Subdominant background yields are taken directly from MC simulation or from additional independent studies in data. For each signal region, a simultaneous "background fit" is performed to the number of events found in the CRs, using a statistical minimisation based on a likelihood implemented in the HistFitter package [102]. In each fit, the normalisations of the background contributions having dedicated CRs are allowed to float, while the MC simulation is used to describe the shape of distributions

of kinematical variables. The agreement of the background prediction with data is compared in dedicated validation regions (VRs), which are not used to constrain the background normalisation or nuisance parameters in the fit.

In order to keep the background normalisation region kinematically as close as possible to the SR, the two-body, three-body and four-body selections use different sets of CRs. The definitions of the regions used in each analysis and the results of the fits are described in the following subsections.

The background due to fake and non-prompt leptons is collectively referred to as "FNP". It consists of semi-leptonic $t\bar{t}$, s-channel and t-channel single top quark, W+jets and light- and heavy-flavour multi-jet events. It is estimated from data with a method similar to that described in Refs. [103, 104]. Two types of lepton identification criteria are defined for this evaluation: "tight" and "loose", corresponding to signal and baseline leptons described in Section 3. The method makes use of the number of observed events containing loose-loose, loose-tight, tight-loose and tight-tight lepton pairs in a given SR. The probability for prompt leptons passing the loose selection criteria to also pass the tight selection is measured using a $Z \rightarrow \ell\ell$ ($\ell = e, \mu$) sample. The equivalent probability for fake or non-prompt leptons is measured in data from multi-jet- and $t\bar{t}$-enriched control samples. The number of events containing a contribution from one or two fake and non-prompt leptons is calculated from these probabilities.

Systematic uncertainties in the samples of simulated events affect the expected yields in the different regions and are taken into account to determine the uncertainties on the background predictions. The systematic uncertainties are described by nuisance parameters, which are not constrained by the fit, since the number of floating background normalisation parameters is equal to the number of the CRs. Each uncertainty source is described by a single nuisance parameter, and all correlations between background processes and selections are taken into account. The list of systematic uncertainties considered in the fits is provided in Section 7.

6.1 Two-body selection background determination

The main background sources for the two-body selection are respectively diboson production in $\text{SRA}_{180}^{2-\text{body}}$ and $t\bar{t}$ and $t\bar{t}$ +Z in $\text{SRB}_{140}^{2-\text{body}}$ and $\text{SRC}_{110}^{2-\text{body}}$. These processes are normalised to data in dedicated CRs described:

- $\text{CR}_{t\bar{t}}^{2-\text{body}}$: this region targets the production of $t\bar{t}$ pairs and selects $t\bar{t}$ events with about 90% purity. It is included in the background fits of $\text{SRA}_{180}^{2-\text{body}}$ and $\text{SRB}_{140}^{2-\text{body}}$.

- $\text{CR}_{t\bar{t},3j}^{2-\text{body}}$: this region targets the production of $t\bar{t}$ pairs and selects $t\bar{t}$ events with about 90% purity. It requires a higher jet multiplicity and is included in the background fit of $\text{SRC}_{110}^{2-\text{body}}$.

- $\text{CR}_{VV-\text{SF}}^{2-\text{body}}$: this region targets the production of a $VV \rightarrow \ell\ell\nu\nu$, where $V = W, Z$, with same flavour lepton pairs. This region selects $VV \rightarrow \ell\ell\nu\nu$ events with about 60% purity. It is included in the background fits of $\text{SRA}_{180}^{2-\text{body}}$ and $\text{SRB}_{140}^{2-\text{body}}$.

14

- $\text{CR}_{t\bar{t}Z}^{2-\text{body}}$: this control region targets the production of $t\bar{t}+Z$ and selects $t\bar{t}+Z$ events with about 60% purity. Events with three charged leptons including one same-flavour opposite-charge pair with $|m_{\ell\ell} - m_Z| < 20$ GeV are selected. In order to mimic the kinematics of the $t\bar{t}+Z$ events with invisible Z decays, a corrected E_T^miss variable, $E_\text{T,corr}^\text{miss}$, is defined by vectorially adding the momentum of the same-flavour opposite-charge lepton pair to the $\mathbf{p}_\text{T}^\text{miss}$. It is included in the background fits of $\text{SRA}_{180}^{2-\text{body}}$, $\text{SRB}_{140}^{2-\text{body}}$ and $\text{SRC}_{110}^{2-\text{body}}$.

- $\text{CR}_{VZ}^{2-\text{body}}$: this control region targets diboson production with more than two final state charged leptons (VZ), with a selection similar to $\text{CR}_{t\bar{t}Z}^{2-\text{body}}$. This region selects the targeted processes with about 85% purity. It is included in the background fits of $\text{SRA}_{180}^{2-\text{body}}$ and $\text{SRB}_{140}^{2-\text{body}}$.

In order to test the reliability of the background prediction, the results of the simultaneous fit are cross-checked in VRs which are disjoint to both the corresponding control and signal regions. The CR and VR definitions are summarised in Table 6. Overlapping regions, e.g. $\text{CR}_{t\bar{t}}^{2-\text{body}}$ and $\text{CR}_{t\bar{t},3j}^{2-\text{body}}$, are only included in independent background fits, so that no correlation is introduced. The expected signal contamination in the CRs is generally below 5%. The highest signal contamination in the VRs, of about 18%, is expected in $\text{VR}_{t\bar{t},3j}^{2-\text{body}}$ for a top squark mass of 400 GeV and a lightest neutralino mass of 175 GeV.

Table 6: *Two-body selection* control and validation regions definition. The common selection defined in Section 4 also applies to all regions but $\text{CR}_{t\bar{t}Z}^{2-\text{body}}$ and $\text{CR}_{VZ}^{2-\text{body}}$, which require three leptons including one same-flavour opposite-charge pair with $|m_{\ell\ell} - m_Z| < 20$ GeV.

	$\text{CR}_{t\bar{t}}^{2-\text{body}}$	$\text{CR}_{t\bar{t},3j}^{2-\text{body}}$	$\text{CR}_{VV-\text{SF}}^{2-\text{body}}$	$\text{CR}_{t\bar{t}Z}^{2-\text{body}}$	$\text{CR}_{VZ}^{2-\text{body}}$	$\text{VR}_{t\bar{t}}^{2-\text{body}}$	$\text{VR}_{t\bar{t},3j}^{2-\text{body}}$	$\text{VR}_{VV-\text{DF}}^{2-\text{body}}$
leptons	2, DF	2	2, SF	3	3	2, DF	2	2, DF
$m_\text{T2}^{\ell\ell}$ [GeV]	[100,120]	[60,100]	[100,120]	–	–	> 120	> 100	[100,120]
$n_{b-\text{jets}}$	≥ 1	≥ 1	0	≥ 2 $\quad$ or $\quad$ = 1	0	≥ 1	≥ 1	≥ 1
n_jets	–	≥ 3	–	≥ 3 $\quad$ or $\quad$ ≥ 4	–	≥ 2	≥ 3	≥ 1
$p_\text{T,boost}^{\ell\ell}$ [GeV]	–	–	< 25	–	–	–	–	< 25
$\Delta\phi_\text{boost}$	–	–	–	–	–	> 1.5	–	–
R_1	–	–	> 0.3	–	–	–	–	–
$E_\text{T,corr}^\text{miss}$ [GeV]	–	–	–	> 120	> 120	–	–	–
E_T^miss [GeV]	–	> 200	–	–	–	–	> 200	–
$R_{\ell\ell}$	–	< 1.2	–	–	–	–	< 1.2	–

Figure 2 shows the distributions of some of the kinematic variables used to define the four control regions after the background fit, so that the plots are illustrating the modelling of the shape of each variable. In general, a good agreement is found between the data and the background model within uncertainties. The other selection variables are equally well described by the background prediction.

The results of the background fits, as well as the MC expected background composition before the fit, are reported in Table 7 for the CRs used in the $\text{SRA}_{180}^{2-\text{body}}$ and $\text{SRB}_{140}^{2-\text{body}}$ background fits and Table 8 for the CRs used in the $\text{SRC}_{110}^{2-\text{body}}$ background fit. The normalisations for fitted backgrounds are found to be consistent with the theoretical predictions, when uncertainties are considered. By construction, in
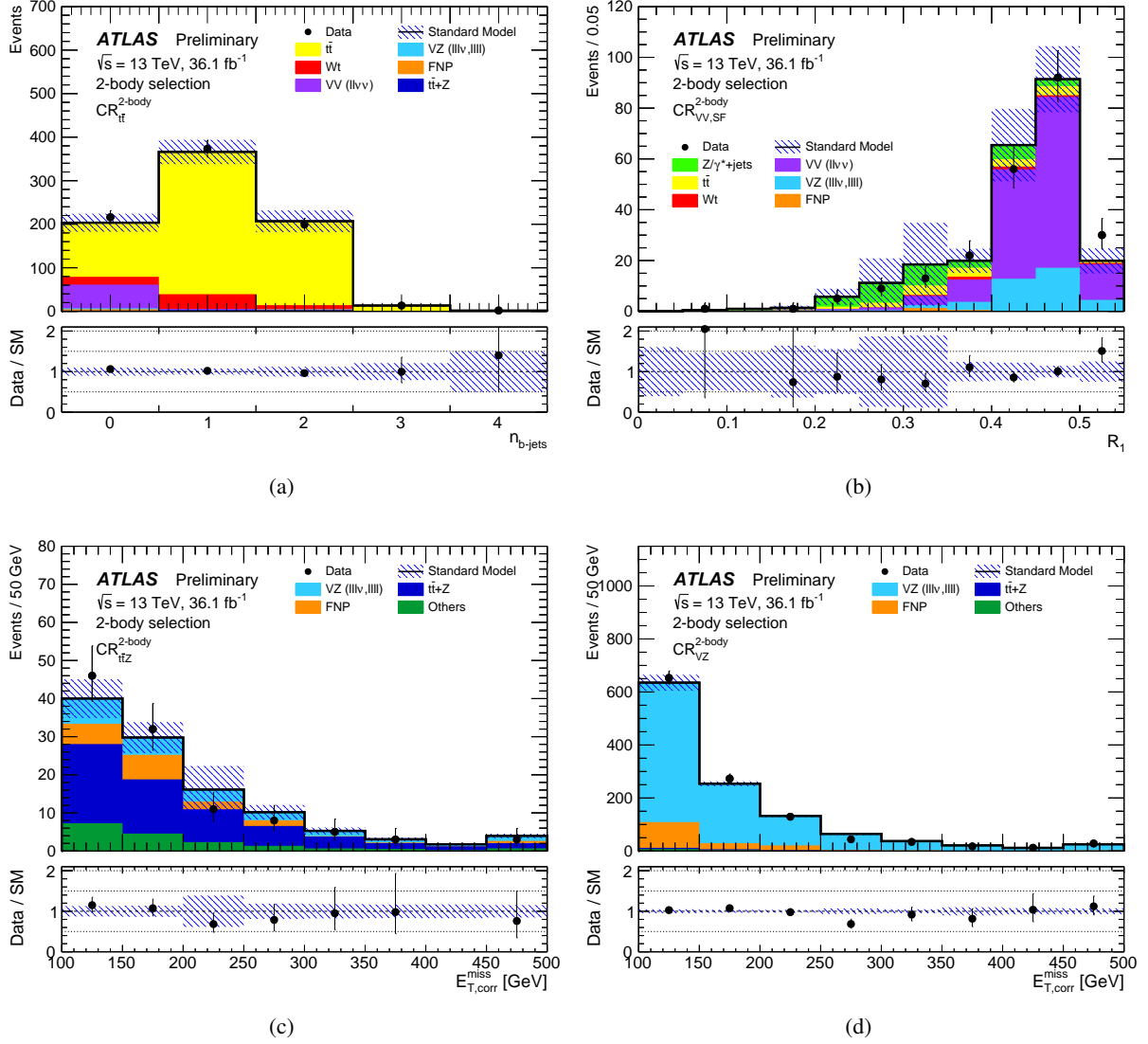
Figure 2: *Two-body selection* distribution of (a) $n_{b-\text{jets}}$ in $\text{CR}_{t\bar{t}}^{2-\text{body}}$, (b) R_1 in $\text{CR}_{VV-\text{SF}}^{2-\text{body}}$ and (c,d) $E_{\text{T,corr}}^{\text{miss}}$ in $\text{CR}_{t\bar{t}Z}^{2-\text{body}}$ and $\text{CR}_{VZ}^{2-\text{body}}$ after the background fits. The contributions from all SM backgrounds are shown as a histogram stack; the bands represent the total statistical and systematic uncertainty. The fake and non-prompt lepton backgrounds are estimated from data, the other backgrounds are estimated from MC simulation with a background fit as described in Section 6. The rightmost bin of each plot includes overflow events.

the CRs the yields observed and predicted by the fits are the same. Good agreement, within one standard deviation from the SM background prediction, is observed in the VRs.

Table 7: *Two-body selection* background fit results for the CRs of the $\mathrm{SRA}^{2-\mathrm{body}}_{180}$ and $\mathrm{SRB}^{2-\mathrm{body}}_{140}$ background fits. The nominal expectations from MC simulation are given for comparison for those backgrounds ($t\bar{t}$, VV-SF, $t\bar{t}Z$ and VZ) that are normalised to data in dedicated CRs. The "Others" category contains the contributions from $t\bar{t}W$, $t\bar{t}h$, $t\bar{t}WW$, $t\bar{t}t$, $t\bar{t}t\bar{t}$, Wh, ggh and Zh production. Combined statistical and systematic uncertainties are given. Events with fake or non-prompt leptons are estimated with the data-driven technique described in Section 6. Entries marked "–" indicate a negligible background contribution. Uncertainties on the predicted background event yields are quoted as symmetric except where the negative uncertainty extends to zero predicted events, in which case the negative uncertainty is truncated.

	$\mathrm{CR}^{2-\mathrm{body}}_{t\bar{t}}$	$\mathrm{CR}^{2-\mathrm{body}}_{VV-\mathrm{SF}}$	$\mathrm{CR}^{2-\mathrm{body}}_{t\bar{t}Z}$	$\mathrm{CR}^{2-\mathrm{body}}_{VZ}$
Observed events	587	213	91	836
Estimated SM Events	587 ± 24	213 ± 15	91 ± 10	836 ± 29
Fit output, $t\bar{t}$	532 ± 25	14 ± 4	–	–
Wt	44 ± 6	4.0 ± 1.5	–	–
Z/γ^* + jets	$0.02^{+0.05}_{-0.02}$	19 ± 10	–	–
Fit output, VV-SF	–	135 ± 18	–	–
VV-DF	2.2 ± 0.8	–	–	–
Fit output, VZ	0.18 ± 0.12	38 ± 7	17.5 ± 2.5	730 ± 50
Fit output, $t\bar{t}$ +Z	2.2 ± 0.8	0.07 ± 0.07	47 ± 12	8.9 ± 2.5
Others	3.8 ± 0.4	0.41 ± 0.18	14.5 ± 1.4	10.3 ± 0.9
Fake and non prompt	1.6 ± 0.9	0^{+5}_{-0}	12 ± 7	86 ± 34
Fit input, $t\bar{t}$	504	14	–	–
Fit input, VV-SF	–	122	–	–
Fit input, VZ	0.18	39	18	735
Fit input, $t\bar{t}$ +Z	3.57	0.08	56	11

Table 8: *Two-body selection* background fit results for the CRs of the $\mathrm{SRC}_{110}^{2-\mathrm{body}}$ background fit. The nominal expectations from MC simulation are given for comparison for those backgrounds ($t\bar{t}$ and $t\bar{t}Z$) that are normalised to data in dedicated CRs. The "Others" category contains the contributions from $t\bar{t}W$, $t\bar{t}h$, $t\bar{t}WW$, $t\bar{t}t$, $t\bar{t}t\bar{t}$, Wh, ggh and Zh production. Combined statistical and systematic uncertainties are given. Events with fake or non-prompt leptons are estimated with the data-driven technique described in Section 6. Entries marked "–" indicate a negligible background contribution. Uncertainties on the predicted background event yields are quoted as symmetric except where the negative uncertainty extends to zero predicted events, in which case the negative uncertainty is truncated.

	$\mathrm{CR}_{t\bar{t},3j}^{2-\mathrm{body}}$	$\mathrm{CR}_{t\bar{t}Z}^{2-\mathrm{body}}$
Observed events	212	91
Estimated SM Events	212 ± 15	91 ± 10
Fit output, $t\bar{t}$	184 ± 16	–
Fit output, $t\bar{t}$ +Z	1.03 ± 0.32	47 ± 12
Wt	23 ± 7	–
VV	1.69 ± 0.30	17.7 ± 2.2
Z/γ^* + jets	0.05 ± 0.02	–
Others	1.91 ± 0.12	14.6 ± 1.0
Fake and non-prompt	–	12 ± 7
Fit input, $t\bar{t}$	201	–
Fit input, $t\bar{t}$ +Z	1.23	55.7

18

6.2 Three-body selection background determination

In the three-body signal regions defined in Section 4.3, the SM background is dominated by diboson and $t\bar{t}$ production. A single control region is used for $t\bar{t}$ production, while two CRs are defined to target diboson events with either same flavour or different flavour lepton pairs. The background predictions are tested in VRs that are defined to be kinematically adjacent to, yet disjoint from, the signal regions. The definitions of the control and validation regions are shown in Table 9. The overlap between $VR_{t\bar{t}}^{3-body}$ and VR_{VV-DF}^{3-body} doesn't affect the final results as these regions are not used for the constraining of the background normalisations. The signal contamination in the CRs and VRs is generally small, with the maximum found to be about 12% in VR_{VV-DF}^{3-body} for a top squark mass of 220 GeV and a lightest neutralino mass of 110 GeV.

Table 9: *Three-body selection* control and validation regions definitions. The common selection defined in Section 4 also applies to all regions.

	$CR_{t\bar{t}}^{3-body}$	CR_{VV-DF}^{3-body}	CR_{VV-SF}^{3-body}	$VR_{t\bar{t}}^{3-body}$	VR_{VV-DF}^{3-body}	VR_{VV-SF}^{3-body}
Lepton flavour	DF	DF	SF	DF	DF	SF
$\|m_{\ell\ell} - m_Z\|$ [GeV]	–	–	> 20	–	–	>20
$n_{b-\mathrm{jets}}$	>0	= 0	= 0	= 0	= 0	= 0
M_{Δ}^{R} [GeV]	> 80	> 50	> 70	> 80	[50, 95]	[60, 95]
$R_{p_{\mathrm{T}}}$	> 0.7	< 0.5	< 0.5	< 0.7	< 0.7	< 0.4
$1/\gamma_{R+1}$	–	> 0.7	> 0.7	–	> 0.7	> 0.7
$(\cos\theta_b, \Delta\phi_{\beta}^{R})$	$\Delta\phi_{\beta}^{R} < (0.9 \times |\cos\theta_b| + 1.6)$			$\Delta\phi_{\beta}^{R} > (0.9 \times |\cos\theta_b| + 1.6)$		

Table 10 shows the expected and observed number of events in each of the control regions after the background fit. The number of total fitted background events in the validation regions is in agreement with the observed number of data events. Figure 3 shows a selected number of distributions in the control regions after the background fit, so that the plots illustrate the MC modelling of the shape of each variable. In general, good agreement between the data and the background model is found within uncertainties. The other selection variables are equally well described by the background prediction. Good agreement, within one standard deviation from the SM background prediction, is observed in the VRs.

Table 10: *Three-body selection* background fit results for the CRs of the $\mathrm{SR}_W^{3-\mathrm{body}}$ and $\mathrm{SR}_t^{3-\mathrm{body}}$ background fit. The nominal expectations from MC simulation are given for comparison for those backgrounds ($t\bar{t}$, VV-DF and VV-SF) that are normalised to data in dedicated CRs. Combined statistical and systematic uncertainties are given. Events with fake or non-prompt leptons are estimated with the data-driven technique described in Section 6. Entries marked "–" indicate a negligible background contribution. Uncertainties on the predicted background event yields are quoted as symmetric except where the negative uncertainty extends to zero predicted events, in which case the negative uncertainty is truncated.

	$\mathrm{CR}_{t\bar{t}}^{3-\mathrm{body}}$	$\mathrm{CR}_{VV-\mathrm{DF}}^{3-\mathrm{body}}$	$\mathrm{CR}_{VV-\mathrm{SF}}^{3-\mathrm{body}}$
Observed events	951	2046	1275
Estimated SM Events	951 ± 31	2046 ± 50	1275 ± 40
Fit output, $t\bar{t}$	833 ± 33	620 ± 110	330 ± 60
Fit output, VV-DF	11.5 ± 2.4	1090 ± 130	–
Fit output, VV-SF	–	–	380 ± 90
Wt	101 ± 10	186 ± 28	103 ± 17
$t\bar{t}+V$	4.3 ± 0.4	0.39 ± 0.06	0.36 ± 0.07
$Z/\gamma*$+jets	0.7 ± 0.22	$1.8^{+2.5}_{-1.8}$	430 ± 50
Higgs	0.31 ± 0.08	79 ± 9	6.2 ± 0.8
Fake and non-prompt	$0.00^{+0.30}_{-0.00}$	65.4 ± 2.2	24.0 ± 1.3
Fit input, $t\bar{t}$	787	590	320
Fit input, VV-DF	11.3	1069	–
Fit input, VV-SF	–	–	370
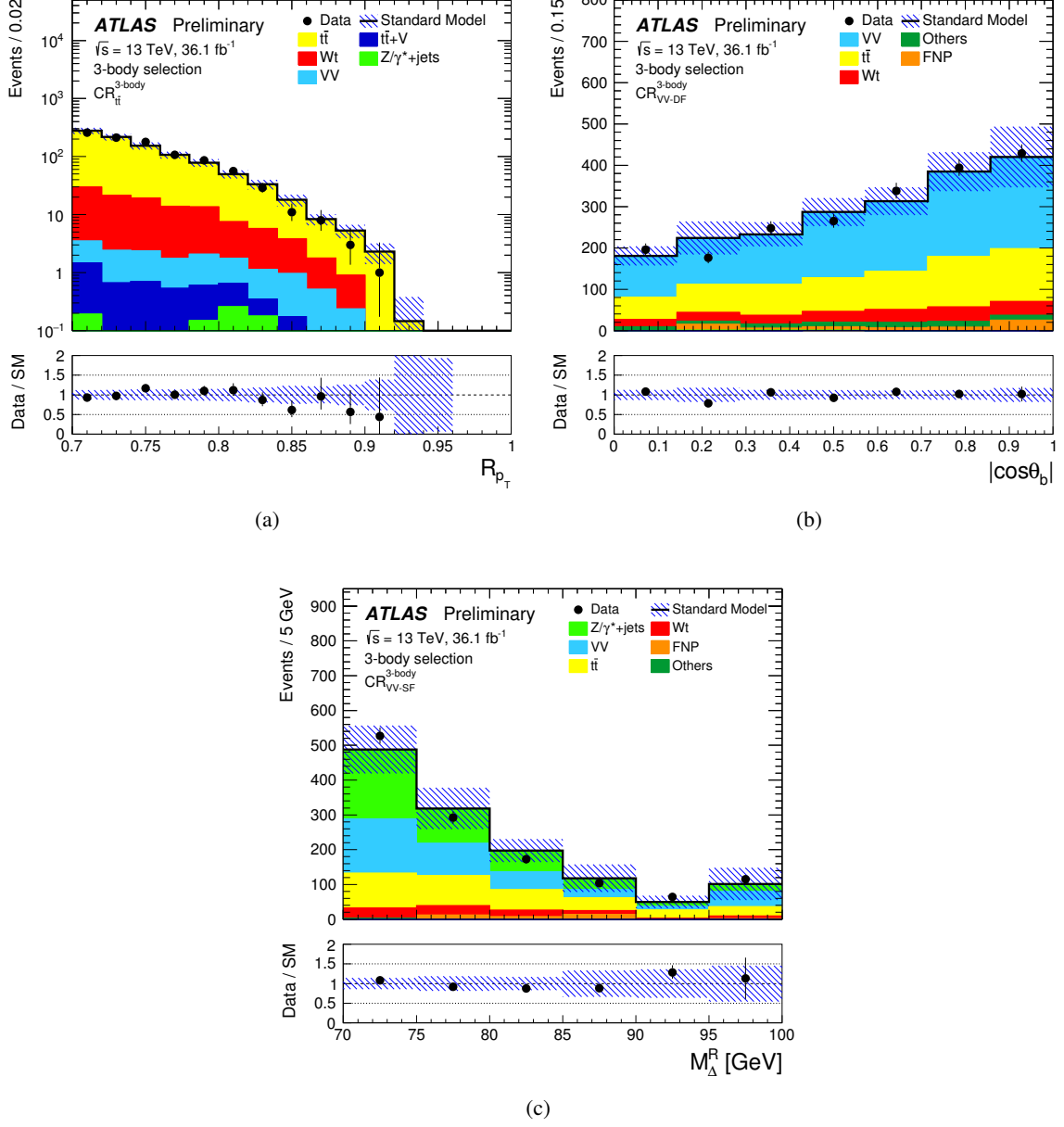
Figure 3: *Three-body selection* distributions of (a) R_{p_T} in $CR_{t\bar{t}}^{3-body}$, (b) $\cos\theta_b$ in CR_{VV-DF}^{3-body}, and (c) M_Δ^R in CR_{VV-SF}^{3-body} after the background fit. The contributions from all SM backgrounds are shown as a histogram stack; the bands represent the total statistical and systematic uncertainty. The fake and non-prompt lepton backgrounds are estimated from data, the other backgrounds are estimated from MC simulation with a background fit as described in Section 6. The rightmost bin of each plot includes overflow events.

6.3 Four-body selection background determination

In the four-body SRs, the largest SM background contributions stem from $t\bar{t}$, diboson production, and the Z boson decaying into $\tau\tau$ with both τ leptons decaying leptonically. Three dedicated control regions are defined: $\mathrm{CR}_{t\bar{t}}^{4-\mathrm{body}}$, $\mathrm{CR}_{VV}^{4-\mathrm{body}}$ and $\mathrm{CR}_{Z\tau\tau}^{4-\mathrm{body}}$. The background predictions are tested in three validation regions that are defined to be kinematically similar, but disjoint, to both the control and signal regions. The definitions of the control and validation regions are shown in Table 11. In the $t\bar{t}$ control region the signal contamination is less than $\sim 6\%$, while in $\mathrm{CR}_{VV}^{4-\mathrm{body}}$ and $\mathrm{CR}_{Z\tau\tau}^{4-\mathrm{body}}$ the highest signal contamination, for a top squark mass of 260 GeV and a lightest neutralino mass of 180 GeV, is respectively $\sim 30\%$ and $\sim 9\%$.

Table 11: *Four-body selection* control and validation regions definition. The common selection reported in Table 4 also applies to all regions.

	$\mathrm{CR}_{t\bar{t}}^{4-\mathrm{body}}$	$\mathrm{CR}_{VV}^{4-\mathrm{body}}$	$\mathrm{CR}_{Z\tau\tau}^{4-\mathrm{body}}$	$\mathrm{VR}_{t\bar{t}}^{4-\mathrm{body}}$	$\mathrm{VR}_{VV}^{4-\mathrm{body}}$	$\mathrm{VR}_{Z\tau\tau}^{4-\mathrm{body}}$
Leading lepton p_T [GeV]	[7,80]	[7,80]	> 20	[7,80]	[7,80]	> 50
Sub-leading lepton p_T [GeV]	[7,35]	[7,35]	> 20	[7,35]	[7,35]	[7,20]
n_jets	≥ 2	= 1	= 1	≥ 2	= 1	= 1
Leading jet p_T [GeV]	[100,150]	> 150	> 150	> 150	> 150	> 150
$m_{\ell\ell}$ [GeV]	> 10	> 45	[10,45]	> 10	> 45	[10,45]
$R_{\ell j}$	-	-	-	< 0.35	-	-
$R_{\ell\ell}$	-	< 5	-	< 12	> 5	-
$n_{b-\mathrm{jets}}$	-	= 0	= 0	-	= 0	= 0

Table 12 shows the expected and observed number of events in each of the control regions after the background fit. Good agreement between data and the SM predictions is observed in the validation regions. Figure 4 shows a selected number of distributions in the control regions for this analysis after applying the normalisation factors provided by the background fit. Good agreement between data and the SM expectations is observed. The other selection variables are equally well described by the background prediction. The largest observed deviation (1.4σ) from the SM background prediction is found in $\mathrm{VR}_{Z\tau\tau}^{4-\mathrm{body}}$. The other VRs yields have been found to be compatible with the SM expectation within one standard deviation.

Table 12: *Four-body selection* background fit results for the CRs of the SR^{4-body} background fit. The nominal expectations from MC simulation are given for comparison for those backgrounds ($t\bar{t}$, VV and $Z_{\tau\tau}$) that are normalised to data in dedicated CRs. Combined statistical and systematic uncertainties are given. Events with fake or non-prompt leptons are estimated with the data-driven technique described in Section 6. Uncertainties on the predicted background event yields are quoted as symmetric except where the negative uncertainty extends to zero predicted events, in which case the negative uncertainty is truncated.

	$CR_{t\bar{t}}^{4-body}$	CR_{VV}^{4-body}	$CR_{Z\tau\tau}^{4-body}$
Observed events	1251	110	106
Estimated SM Events	1251 ± 35	110 ± 10	106 ± 10
Fit output, $t\bar{t}$	960 ± 50	47 ± 20	10 ± 6
Fit output, VV	37 ± 22	40 ± 22	18 ± 11
Fit output, $Z_{\tau\tau}$	22 ± 8	$0.00^{+0.17}_{-0.00}$	54 ± 16
$t\bar{t}$ +Z	5.6 ± 0.8	0.08 ± 0.01	0.05 ± 0.02
Wt	62 ± 19	9.0 ± 2.7	2.7 ± 2.4
Z_{ee}, $Z_{\mu\mu}$	0.7 ± 0.5	$0.2^{+0.4}_{-0.2}$	1.6 ± 0.6
Others	11.2 ± 1.6	0.51 ± 0.12	3.2 ± 0.6
Fake and non-prompt	154 ± 14	13.1 ± 2.0	16 ± 7
Fit input, $t\bar{t}$	931	46	10
Fit input, VV	47	51	23
Fit input, $Z_{\tau\tau}$	20	0	51

23
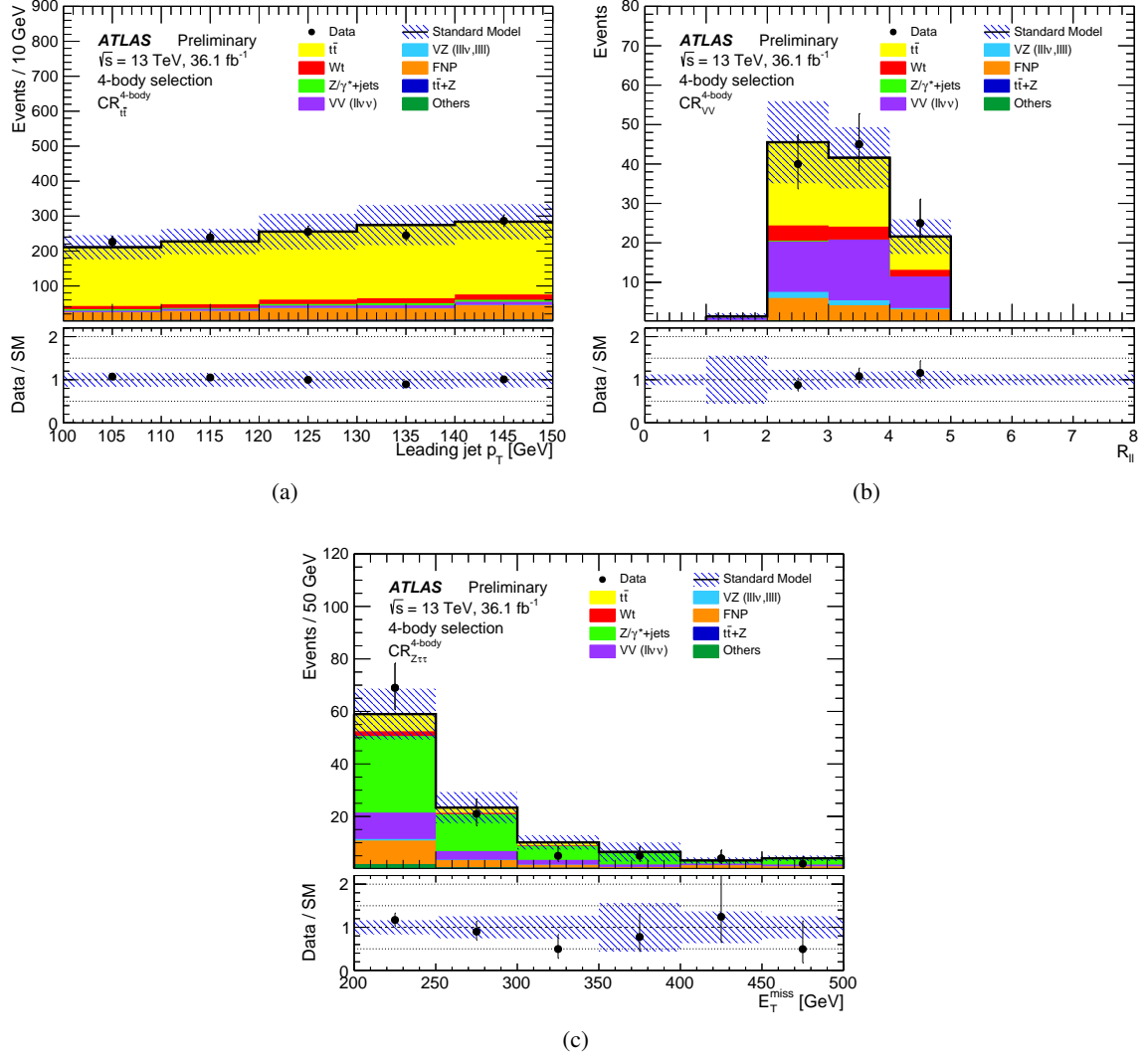
Figure 4: *Four-body selection* distributions of the (a) $p_T(j_1)$ in $CR_{t\bar{t}}^{4-body}$, (b) $R_{\ell\ell}$ in CR_{VV}^{4-body} and (c) E_T^{miss} in $CR_{Z\tau\tau}^{4-body}$ after the background fit. The contributions from all SM backgrounds are shown as a histogram stack; the bands represent the total statistical and systematic uncertainty. The fake and non-prompt lepton backgrounds are estimated from data, the other backgrounds are estimated from MC simulation with a background fit as described in Section 6. The rightmost bin of each plot includes overflow events.

7 Systematic uncertainties

The primary sources of systematic uncertainties are related to: the jet energy scale (JES), jet energy resolution (JER), and the theoretical and MC modelling uncertainties on the backgrounds determined using CRs. The statistical uncertainties of the simulated event samples are also taken into account. The effect of the systematic uncertainties is evaluated for all signal samples and background processes. Since the normalisation of the dominant background processes is extracted in dedicated control regions, the systematic uncertainties only affect the extrapolation to the signal regions in these cases. Uncertainties due to the limited number of events in the CRs are also introduced in the fit for each region.

The JES and JER uncertainties are derived as a function of the p_T and η of the jet, as well as of the pile-up conditions and the jet flavour composition of the selected jet sample [46]. Uncertainties associated to the modelling of the b-tagging efficiencies for b, c and light-flavour jets [105, 106] are also considered.

The systematic uncertainties related to the modelling of E_T^{miss} in the simulation are estimated by propagating the uncertainties on the energy and momentum scale of each of the physics objects, as well as the uncertainties on the soft term resolution and scale [52].

Other detector-related systematic uncertainties, such as those on lepton reconstruction efficiency, energy scale, energy resolution and on the modelling of the trigger efficiency [40, 41], are found to have a small impact on the results and are generally negligible with respect to the other detector related uncertainties.

The uncertainties on the modelling of the $t\bar{t}$ and single-top backgrounds in simulation are estimated by varying the renormalisation and factorisation scales, as well as the amount of initial- and final-state radiation used to generate the samples [59]. Uncertainties on the parton shower modelling are assessed as the difference between the predictions from Powheg showered with Pythia and Herwig, and on the generator choice by comparing Powheg and MadGraph5_aMC@NLO [59]. The uncertainty on the interference between $t\bar{t}$ and single top quark Wt production is assigned by comparing the predictions of dedicated LO MadGraph 2.5 samples. The predictions for $t\bar{t}$ and Wtb are compared with the $WWbb$ process, where the same production diagrams are included, but top quarks are not required to be on-shell.

The diboson background MC modelling uncertainties are estimated by varying up and down by a factor of two the renormalisation, factorisation and resummation scales used to generate the sample [107]. For $t\bar{t}Z$ production, the predictions from the MadGraph5_aMC@NLO and Sherpa generators are compared, and the uncertainties related to the choice of the renormalisation and factorisation scales are assessed by varying the corresponding generator parameters up and down by a factor of two around their nominal values [108].

The uncertainties related to the choice of the QCD renormalisation and factorisation scales in $Z/\gamma^* +$ jets events are assessed by varying the corresponding generator parameters up and down by a factor of two around their nominal values. Uncertainties on the choice of the resummation scale and the matching scale between the matrix element and the parton shower are evaluated by varying up and down by a factor of two the corresponding parameters in Sherpa.

The cross-sections used to normalise the MC samples are varied according to the uncertainty on the cross-section calculation, that is, 5.3% uncertainty for single top quark Wt-channel [109], 6% for diboson, 13% for $t\bar{t}W$ and 12% for $t\bar{t}Z$ production [64]. For $t\bar{t}WW$, tZ, tWZ, $t\bar{t}h$, $t\bar{t}t$, $t\bar{t}t\bar{t}$, and tribosons production processes, which constitute a small background, a 50% uncertainty on the event yields is assumed.

Systematic uncertainties are assigned to the FNP background estimate to account for potentially different compositions (heavy flavour, light flavour or conversions) between the signal and control regions, as well for the contamination from prompt leptons in the regions used to measure the probabilities for loose fake and non-prompt leptons to pass the tight signal criteria. Parameterisations of these probabilities are independently derived from $t\bar{t}$- and multi-jet-enriched same charge dilepton samples. The $t\bar{t}$ enriched sample is used to derive the parameterisation from which the central prediction for the FNP background is obtained. The full difference between the prediction derived from the $t\bar{t}$ and the multi-jet parameterisation is assigned as systematic uncertainty on the central FNP prediction and symmetrised.

A 3.2% uncertainty in the luminosity measurement is also taken into consideration for all signal and background estimates that are directly derived from MC simulations.

Table 13 summarises the contributions of the different sources of systematic uncertainty in the total SM background predictions in the signal regions. The total systematic uncertainty ranges between 15% and 46%, with the dominant sources being the MC statistics, the JES and E_T^{miss} modelling, the statistics in the CRs and the $t\bar{t}$ theoretical uncertainties.

Table 13: Sources of systematic uncertainty on the SM background estimates, evaluated after the background fits. The values are given as relative uncertainties on the total expected background event yields in the SRs. Entries marked "–" indicate either a negligible contribution or an uncertainty that does not apply (for example the normalisation uncertainty for a background whose normalisation is not fitted for that specific signal region). MC statistics refer to the statistical uncertainty from the simulated event samples. The individual components can be correlated and therefore do not necessarily add up in quadrature to the total systematic uncertainty.

Signal Region	SRA$^{2-body}_{180}$ SF	SRA$^{2-body}_{180}$ DF	SRB$^{2-body}_{140}$ SF	SRB$^{2-body}_{140}$ DF	SRC$^{2-body}_{110}$ SF	SRC$^{2-body}_{110}$ DF	SR$^{3-body}_{W}$ SF	SR$^{3-body}_{W}$ DF	SR$^{3-body}_{t}$ SF	SR$^{3-body}_{t}$ DF	SR^{4-body} DF
Total SM background uncertainty	21%	32%	15%	21%	35%	38%	36%	39%	46%	42%	20%
Diboson theoretical uncertainties	4.0%	5.9%	–	–	–	–	9.1%	10%	1.3%	–	2.7%
$t\bar{t}$ theoretical uncertainties	–	–	4.2%	6.6%	12%	13%	13%	18%	25%	24%	8.1%
Wt theoretical uncertainties	–	–	1.8%	1.9%	–	5.4%	–	–	–	–	–
$t\bar{t}$-Wt interference	–	–	–	7.9%	–	–	–	–	–	–	–
MC statistical uncertainties	13%	28%	12%	13%	15%	15%	16%	14%	20%	22%	10%
VV normalisation	14%	–	–	–	–	–	12%	4.3%	1.3%	–	9.2%
$t\bar{t}$ normalisation	–	–	–	–	16%	15%	1.8%	2.5%	3.5%	3.5%	8.6%
$t\bar{t}$+Z normalisation	–	–	7.6%	9.9%	8.5%	10%	–	–	–	–	–
$Z_{\tau\tau}$ normalisation	–	–	–	–	–	–	–	–	–	–	1.5%
Jet energy scale	6.9%	3.1%	4.1%	6.4%	13%	22%	19%	18%	27%	11%	4.4%
Jet energy resolution	–	13%	2.2%	3.2%	12%	16%	7.2%	18%	2.9%	22%	1.0%
E_{T}^{miss} modelling	5.0%	–	3.0%	1.5%	26%	23%	18%	11%	14%	6.5%	1.3%
b-tagging	–	–	1.1%	4.3%	–	–	2.7%	3.0%	1.0%	3.0%	2.2%
Pile-up reweighting	2.0%	3.2%	–%	1.1%	2.9%	4.6%	2.9%	5.0%	5.1%	4.9%	1.4%
Lepton modelling	1.3%	2.1%	7.4%	1.1%	–	–	1.1%	3.1%	4.6%	3.0%	2.5%
Fake and non-prompt leptons	–	–	–	–	4.0%	–	2.8%	–	–	–	14%

8 Results

The data are compared to background predictions in the signal regions of the different selections. Good agreement is observed between data and the SM background predictions.

8.1 Two-body results

Figure 5 shows the $m_{\text{T2}}^{\ell\ell}$ distribution in each of the two-body signal regions, split between the same and different lepton flavour channels, omitting the selection on $m_{\text{T2}}^{\ell\ell}$ itself. The estimated SM yields in $\text{SRA}_{180}^{2-\text{body}}$ and $\text{SRB}_{140}^{2-\text{body}}$ are determined with a background fit simultaneously determining the normalisations of $t\bar{t}$, SF diboson production, $t\bar{t}+Z$ and diboson production with more than two charged leptons by including $\text{CR}_{t\bar{t}}^{2-\text{body}}$, $\text{CR}_{VV-\text{SF}}^{2-\text{body}}$, $\text{CR}_{t\bar{t}Z}^{2-\text{body}}$ and $\text{CR}_{VZ}^{2-\text{body}}$ in the likelihood minimisation. The estimated SM yields in $\text{SRC}_{110}^{2-\text{body}}$ are determined with a background fit simultaneously determining the normalisations of $t\bar{t}$ and $t\bar{t}+Z$ by including $\text{CR}_{t\bar{t},3j}^{2-\text{body}}$ and $\text{CR}_{t\bar{t}Z}^{2-\text{body}}$ in the likelihood minimisation. No significant excess over the SM prediction is observed, as can be seen from the background-only fit results which are shown in Table 14 for $\text{SRA}_{180}^{2-\text{body}}$ and $\text{SRB}_{140}^{2-\text{body}}$ and Table 15 for the $\text{SRC}_{110}^{2-\text{body}}$. Table 16 reports the observed and expected yields for the SRs used for the computation of the exclusion limits.

Table 14: *Two-body selection* background fit results for $\mathrm{SRA}^{2-\mathrm{body}}_{180}$ and $\mathrm{SRB}^{2-\mathrm{body}}_{140}$. The nominal expectations from MC simulation are given for comparison for those backgrounds ($t\bar{t}$, VV-SF, $t\bar{t}Z$ and VZ) that are normalised to data in dedicated CRs. The "Others" category contains the contributions from $t\bar{t}W$, $t\bar{t}h$, $t\bar{t}WW$, $t\bar{t}t$, $t\bar{t}t\bar{t}$, Wh, ggh and Zh production. Combined statistical and systematic uncertainties are given. Events with fake or non-prompt leptons are estimated with the data-driven technique described in Section 6. Entries marked "–" indicate a negligible background contribution. Uncertainties on the predicted background event yields are quoted as symmetric except where the negative uncertainty extends to zero predicted events, in which case the negative uncertainty is truncated. The "Others" contribution to $\mathrm{SRB}^{2-\mathrm{body}}_{140}$ is dominated by $t\bar{t}W$.

|	$\mathrm{SRA}^{2-\mathrm{body}}_{180}$ SF	$\mathrm{SRA}^{2-\mathrm{body}}_{180}$ DF	$\mathrm{SRB}^{2-\mathrm{body}}_{140}$ SF	$\mathrm{SRB}^{2-\mathrm{body}}_{140}$ DF
Observed events	16	8	9	7
Estimated SM Events	12.3 ± 2.6	5.4 ± 1.7	7.4 ± 1.1	4.8 ± 1.0
Fit output, $t\bar{t}$	–	–	0.8 ± 0.4	0.8 ± 0.5
Wt events	–	–	0.38 ± 0.29	0.7 ± 0.5
Z/γ^* + jets	0.35 ± 0.21	–	1.24 ± 0.32	0.03 ± 0.01
Fake and non prompt	$0.00^{+0.30}_{-0.00}$	$0.00^{+0.30}_{-0.00}$	0.8 ± 0.5	$0.00^{+0.30}_{-0.00}$
VV-DF	–	4.5 ± 1.5	–	0.23 ± 0.06
Fit output, VV-SF	9.8 ± 2.5	–	0.39 ± 0.11	–
Fit output, VZ	1.91 ± 0.31	0.52 ± 0.17	0.53 ± 0.14	0.04 ± 0.01
Fit output, $t\bar{t} + Z$	0.08 ± 0.03	0.15 ± 0.06	2.3 ± 0.6	1.8 ± 0.5
Others	0.18 ± 0.02	0.24 ± 0.07	1.10 ± 0.16	1.11 ± 0.16
Fit input, $t\bar{t}$	–	–	0.78	0.8
Fit input, VV-SF	8.8	–	0.35	–
Fit input, VZ	1.9	0.52	0.54	0.04
Fit input, $t\bar{t} + Z$	0.09	0.17	2.6	2.2
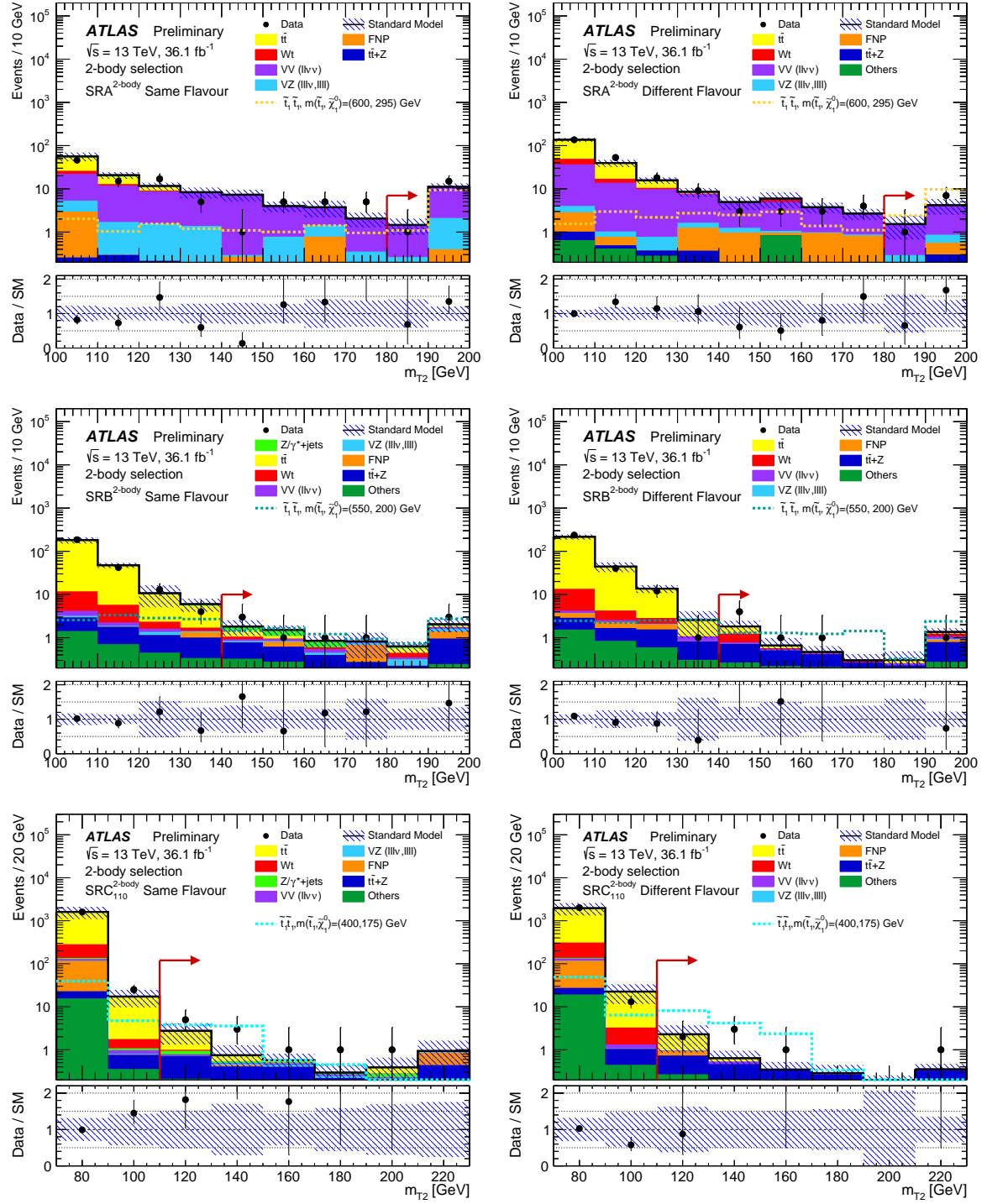
Figure 5: *Two-body selection* distributions of $m_{T2}^{\ell\ell}$ for events satisfying the selection criteria of the six SRs, except for the one on $m_{T2}^{\ell\ell}$, after the background fit. The contributions from all SM backgrounds are shown as a histogram stack; the bands represent the total statistical and systematic uncertainty. The fake and non-prompt lepton backgrounds are estimated from data, the other backgrounds are estimated from MC simulation with a background fit as described in Section 6. The rightmost bin of each plot includes overflow events. Reference top squark pair production signal models are overlaid for comparison. Red arrows indicate the signal region selection criteria.

Table 15: *Two-body selection* background fit results for SRC_{110}^{2-body}. The nominal expectations from MC simulation are given for comparison for those backgrounds ($t\bar{t}$ and $t\bar{t}Z$) that are normalised to data in dedicated CRs. The "Others" category contains the contributions from $t\bar{t}W$, $t\bar{t}h$, $t\bar{t}WW$, $t\bar{t}t$, $t\bar{t}t\bar{t}$, Wh, ggh and Zh production. Combined statistical and systematic uncertainties are given. Events with fake or non-prompt leptons are estimated with the data-driven technique described in Section 6. Entries marked "–" indicate a negligible background contribution. Uncertainties on the predicted background event yields are quoted as symmetric except where the negative uncertainty extends to zero predicted events, in which case the negative uncertainty is truncated.

	SRC_{110}^{2-body} SF	SRC_{110}^{2-body} DF
Observed events	11	7
Estimated SM Events	5.3 ± 1.8	3.8 ± 1.5
Fit output, $t\bar{t}$	2.1 ± 1.3	1.4 ± 1.2
Fit output, $t\bar{t}$ +Z	1.6 ± 0.5	1.4 ± 0.5
Wt	$0.05^{+0.09}_{-0.05}$	$0.00^{+0.23}_{-0.00}$
$VV+VZ$	0.33 ± 0.06	0.12 ± 0.04
$Z/\gamma^* +$ jets	$0.3^{+0.5}_{-0.3}$	–
Others	0.67 ± 0.13	0.81 ± 0.15
Fake and non-prompt	$0.18^{+0.41}_{-0.18}$	$0.00^{+0.02}_{-0.00}$
Fit input, $t\bar{t}$	2.3	1.6
Fit input, $t\bar{t}$ +Z	1.9	1.70

Table 16: *Two-body selection* background fit results for $SR(A, B)_{x,y}^{2-body}$ regions, where x and y denote the low and high edges of the bin. Combined statistical and systematic uncertainties are given. Uncertainties on the predicted background event yields are quoted as symmetric.

	Lepton flavour	$SRA_{120,140}^{2-body}$	$SRB_{120,140}^{2-body}$	$SRA_{140,160}^{2-body}$	$SRA_{160,180}^{2-body}$
Observed events	SF	22	17	6	10
Estimated SM Events		20.0 ± 4.6	16.3 ± 6.2	11.0 ± 2.5	5.6 ± 1.8
Observed events	DF	27	13	6	7
Estimated SM Events		23.8 ± 4.2	16.1 ± 5.3	10.8 ± 2.1	6.4 ± 1.3

8.2 Three-body results

Figure 6 shows the distributions of R_{p_T} and M_Δ^R in each of the signal regions, split between the same and different flavour channels, omitting the cut on R_{p_T} and on M_Δ^R. The estimated SM yields in SR_W^{3-body} and SR_t^{3-body} are determined with a background fit simultaneously determining the normalisations of $t\bar{t}$, SF diboson production and DF diboson production by including $CR_{t\bar{t}}^{3-body}$, CR_{VV-SF}^{3-body} and CR_{VV-DF}^{3-body} in the likelihood minimisation. No excess over the SM prediction is observed. Table 17 shows the background fit results.

Table 17: *Three-body selection* background fit results for SR_W^{3-body} and SR_t^{3-body}. The nominal expectations from MC simulation are given for comparison for those backgrounds ($t\bar{t}$, VV-DF and VV-SF) that are normalised to data in dedicated CRs. Combined statistical and systematic uncertainties are given. Events with fake or non-prompt leptons are estimated with the data-driven technique described in Section 6. Entries marked "–" indicate a negligible background contribution. Uncertainties on the predicted background event yields are quoted as symmetric except where the negative uncertainty extends to zero predicted events, in which case the negative uncertainty is truncated.

|	SR_W^{3-body} SF	SR_W^{3-body} DF	SR_t^{3-body} SF	SR_t^{3-body} DF
Observed events	4	6	6	6
Estimated SM Events	9.8 ± 3.4	7.8 ± 3.0	3.1 ± 1.4	4.4 ± 1.8
Fit output, $t\bar{t}$	4.2 ± 1.6	4.6 ± 2.1	2.5 ± 1.3	3.6 ± 1.8
Fit output, VV-DF	–	2.9 ± 1.4	–	0.04 ± 0.03
Fit output, VV-SF	3.4 ± 2.1	–	0.16 ± 0.08	–
Wt	0.31 ± 0.22	0.23 ± 0.12	0.12 ± 0.05	0.14 ± 0.08
$t\bar{t}+V$	0.03 ± 0.01	0.06 ± 0.02	0.18 ± 0.04	0.24 ± 0.07
$Z/\gamma*$+jets	1.5 ± 0.7	0.05 ± 0.01	0.1 ± 0.03	0.0 ± 0.0
Fake and non-prompt	0.42 ± 0.28	0.06 ± 0.06	$0.00^{+0.30}_{-0.00}$	0.41 ± 0.09
Fit input, $t\bar{t}$	4.0	4.3	2.4	3.4
Fit input, VV-DF	–	2.8	–	0.04
Fit input, VV-SF	3.4	–	0.16	–
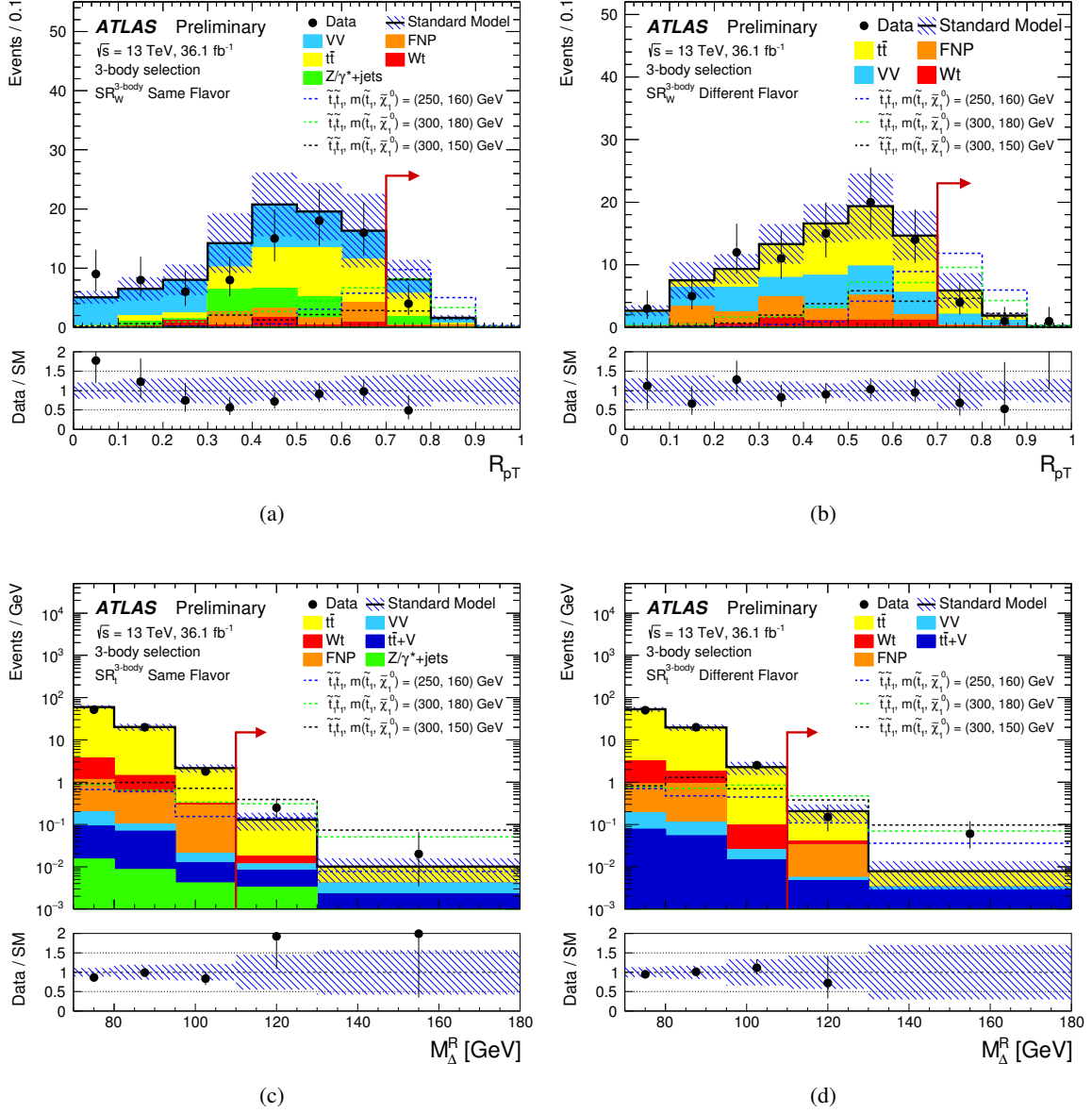
Figure 6: *Three-body selection* distributions of R_{p_T} in same flavour (a) and different flavour (b) events that satisfy all the SR_W^{3-body} selection criteria except for the one on R_{p_T}, and of M_Δ^R in the same flavour (c) and different flavour (d) events that satisfy all the SR_t^{3-body} selection criteria except for the one on M_Δ^R after the background fit. The contributions from all SM backgrounds are shown as a histogram stack; the bands represent the total statistical and systematic uncertainty. The fake and non-prompt lepton backgrounds are estimated from data, the other backgrounds are estimated from MC simulation with a background fit as described in Section 6. The rightmost bin of each plot includes overflow events. Reference top squark pair production signal models are overlaid for comparison. Red arrows indicate the signal region selection criteria.

8.3 Four-body results

Figure 7 shows the distributions of $R_{\ell j}$ and $R_{\ell \ell}$ for events satisfying all the SR$^{4-\text{body}}$ selections. No significant excess over the SM prediction is visible. The estimated SM yields in SR$^{4-\text{body}}$ are determined with a background fit simultaneously determining the normalisations of $t\bar{t}$, diboson production, and Z/γ^*+jets where $Z \to \tau\tau$, by including CR$_{t\bar{t}}^{4-\text{body}}$, CR$_{VV}^{4-\text{body}}$ and CR$_{Z\tau\tau}^{4-\text{body}}$ in the likelihood minimisation. The background fit results are shown in Table 18. The observed yield is within less than one standard deviation of the background prediction in the SR.
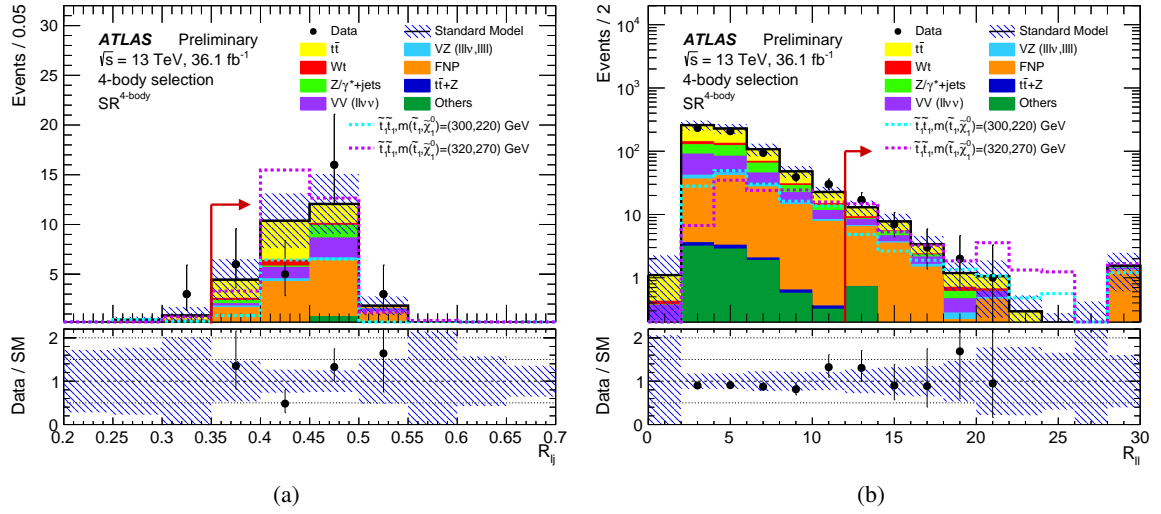
Figure 7: *Four-body selection* distributions of $R_{\ell j}$ (a), $R_{\ell \ell}$ (b) for events satisfying all the SR$^{4-\text{body}}$ selections but for the one on the variable shown in the figure, after the background fit. The contributions from all SM backgrounds are shown as a histogram stack; the bands represent the total statistical and systematic uncertainty. The fake and non-prompt lepton backgrounds are estimated from data, the other backgrounds are estimated from MC simulation with a background fit as described in Section 6. The rightmost bin of each plot includes overflow events. Reference top squark pair production signal models are overlayed for comparison. Red arrows indicate the signal region selection criteria.

Table 18: *Four-body selection* background fit results for SR^{4-body}. The nominal expectations from MC simulation are given for comparison for those backgrounds ($t\bar{t}$, VV and $Z_{\tau\tau}$) that are normalised to data in dedicated CRs. The "Others" category contains the contributions from $t\bar{t}W$, $t\bar{t}h$, $t\bar{t}WW$, $t\bar{t}t$, $t\bar{t}t\bar{t}$, Wh, ggh and Zh production. Combined statistical and systematic uncertainties are given. Events with fake or non-prompt leptons are estimated with the data-driven technique described in Section 6. Entries marked "–" indicate a negligible background contribution. Uncertainties on the predicted background event yields are quoted as symmetric except where the negative uncertainty extends to zero predicted events, in which case the negative uncertainty is truncated.

	SR^{4-body}
Observed events	30
Estimated SM Events	28 ± 6
Fit output, $t\bar{t}$	7.9 ± 2.0
Fit output, VV	4.5 ± 2.3
Fit output, $Z_{\tau\tau}$	1.2 ± 0.6
$t\bar{t}$ +Z	0.03 ± 0.01
Wt	1.08 ± 0.27
$Z_{ee}, Z_{\mu\mu}$	0.21 ± 0.09
Others	0.80 ± 0.30
Fake and non-prompt	12.8 ± 4.3
Fit input, $t\bar{t}$	7.7
Fit input, VV	5.7
Fit input, $Z_{\tau\tau}$	1.1

8.4 Interpretation

Two different sets of exclusion limits are derived on models of new physics beyond the SM. A model-independent upper limit on the visible cross-section σ_{vis} of new physics, defined as cross-section times acceptance times efficiency, is derived in each SR by performing a fit which includes the observed yield in the SR as a constraint, and a free signal yield in the SR as an additional process. The CLs method [110] is used to derive all the exclusion confidence levels. These limits assume negligible signal contamination in the CRs. Model independent upper limits at 95% CL are presented in Table 19.

Model dependent limits are computed on various $\tilde{t}_1$ pair production scenarios. Profile likelihood fits are performed including the expected signal yield and its associated uncertainties in the CRs and SRs. All limits are quoted at 95% CL. When setting limits, the regions included in the $m_{\mathrm{T2}}^{\ell\ell}$ shape fits ($SRA_{x,y}^{2-body}$ and $SRB_{x,y}^{2-body}$) are statistically combined. Similarly, the SR_W^{3-body} and SR_t^{3-body} signal regions are statistically combined as well. For each signal model the SR with the best expected limit is considered.

Limits for simplified models in which pair-produced $\tilde{t}_1$ decay with 100% branching ratio into a top quark and $\tilde{\chi}_1^0$ are shown in the $\tilde{t}_1$–$\tilde{\chi}_1^0$ mass plane in Figure 8. The various SRs cover the different $\tilde{t}_1$ mass ranges, as described in Table 1. Top squark masses up to 720 GeV are excluded for a massless lightest neutralino. Neutralino masses up to 300 GeV are excluded for $m_{\tilde{t}_1}$ = 645 GeV. In the three-body decay hypothesis,

top squark masses are excluded up to 430 GeV for $m_{\tilde{t}_1} - m_{\tilde{\chi}_1^0}$ close to the W boson mass. In the four-body decay hypothesis, top squark masses are excluded up to 400 GeV for $m_{\tilde{t}_1} - m_{\tilde{\chi}_1^0} = 40$ GeV.

Limits are shown for a class of simplified models in which only pair-produced $\tilde{t}_1$ decaying with 100% branching ratio into the lightest chargino and a b-quark are considered. Figure 9 shows the interpretation in the $\tilde{t}_1$–$\tilde{\chi}_1^0$ mass plane assuming that $m_{\tilde{t}_1} - m_{\tilde{\chi}_1^\pm} = 10$ GeV. Top squark masses up to 700 GeV are excluded for an LSP mass up to 200 GeV.

Finally, limits are set on a pMSSM model where the wino and bino mass parameters, M_1 and M_2, are set to $M_2 = 2M_1$ and $m_{\tilde{t}_1} > m_{\tilde{\chi}_1^\pm}$. The remaining pMSSM parameters [20, 21] have the following values: $M_3 = 2.2$ TeV (gluino mass parameter), $M_S = \sqrt{\tilde{t}_1\tilde{t}_2} = 1.2$ TeV (product of top squark masses), $X_t/M_S = \sqrt{6}$ (mixing parameter between the left- and right-handed states), and $\tan\beta = 20$ (ratio of vacuum expectation values of the two Higgs doublets). Limits are set for both positive and negative values of μ (the Higgs mass parameter) as a function of $m_{\tilde{t}_1}$ and $m_{\tilde{\chi}_1^0}$, and are shown in Figure 10. Top squark masses up to about 700 GeV are excluded for a lightest neutralino of about 280 GeV. The sensitivity for low values of $m_{\tilde{\chi}_1^0}$ is limited by the $m_{T2}^{\ell\ell}$ selection acceptance, since $m_{\tilde{\chi}_1^\pm} - m_{\tilde{\chi}_1^0}$ is reduced by the assumption of $M_2 = 2M_1$.

Table 19: Model-independent 95% CL upper limits on the visible cross-section (σ_{vis}) of new physics, the visible number of signal events (S_{obs}^{95}), the visible number of signal events (S_{exp}^{95}) given the expected number of background events (and $\pm 1\sigma$ excursions on the expectation), and the discovery p-value ($p(s = 0)$), all calculated with pseudo-experiments, are shown for each SR.

|	Signal Region	σ_{vis} [fb]	S_{obs}^{95}	S_{exp}^{95}	$p(s = 0)$
two-body	$\mathrm{SRA}_{180}^{2-\mathrm{body}}$ SF	0.37	13.2	10^{+4}_{-3}	0.20
	$\mathrm{SRA}_{180}^{2-\mathrm{body}}$ DF	0.26	9.5	$7.0^{+3.0}_{-1.8}$	0.19
	$\mathrm{SRB}_{140}^{2-\mathrm{body}}$ SF	0.24	8.6	$7.2^{+2.7}_{-1.8}$	0.28
	$\mathrm{SRB}_{140}^{2-\mathrm{body}}$ DF	0.23	8.4	$6.0^{+2.7}_{-1.3}$	0.19
	$\mathrm{SRC}_{110}^{2-\mathrm{body}}$ SF	0.36	13.0	$7.4^{+3.1}_{-2.0}$	0.05
	$\mathrm{SRC}_{110}^{2-\mathrm{body}}$ DF	0.26	9.5	$6.3^{+2.5}_{-1.6}$	0.12
three-body	$\mathrm{SR}_W^{3-\mathrm{body}}$-SF	0.17	6.1	9^{+4}_{-2}	0.72
	$\mathrm{SR}_W^{3-\mathrm{body}}$-DF	0.21	7.5	$8.5^{+3.5}_{-2.0}$	0.85
	$\mathrm{SR}_t^{3-\mathrm{body}}$-SF	0.24	8.8	$6.0^{+2.4}_{-1.4}$	0.12
	$\mathrm{SR}_t^{3-\mathrm{body}}$-DF	0.23	8.2	$6.6^{+2.8}_{-1.6}$	0.28
four-body	$\mathrm{SR}^{4-\mathrm{body}}$	0.48	17.4	16^{+7}_{-5}	0.37
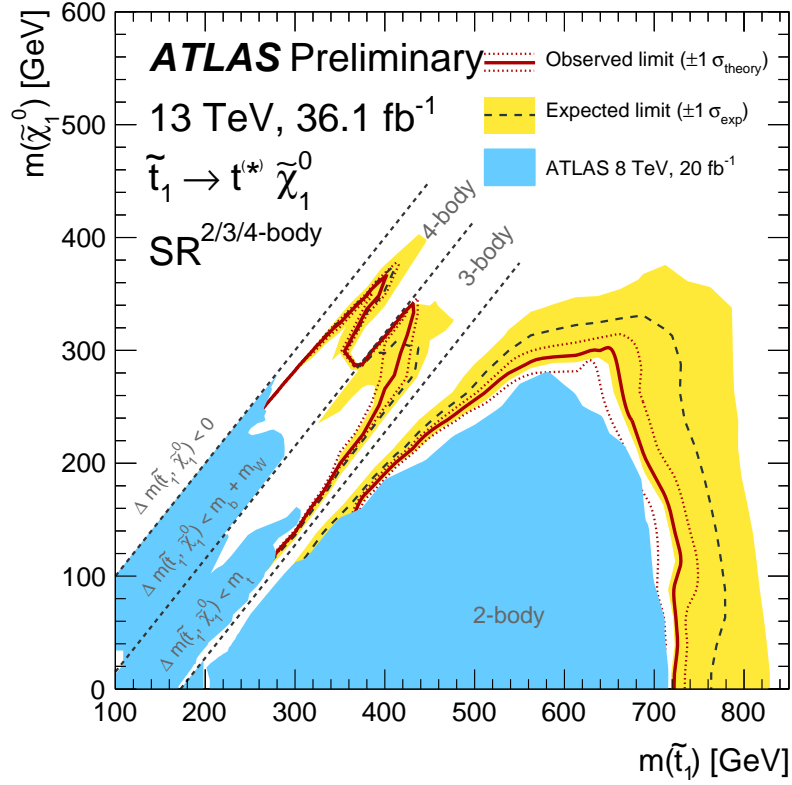
Figure 8: Exclusion contour for a simplified model assuming $\tilde{t}_1$ pair production, decaying via $\tilde{t}_1 \to t\tilde{\chi}_1^0$ with 100% branching ratio. The dashed grey line and the shaded band are the expected limit and its $\pm 1\sigma$ uncertainty. The thick solid red line is the observed limit for the central value of the signal cross-section. The expected and observed limits do not include the effect of the theoretical uncertainties on the signal cross-section. The dotted lines show the effect on the observed limit when varying the signal cross-section by $\pm 1\sigma$ of the theoretical uncertainty. The shaded blue areas show respectively the observed exclusion from the ATLAS $\sqrt{s} = 8$ TeV analyses [22].
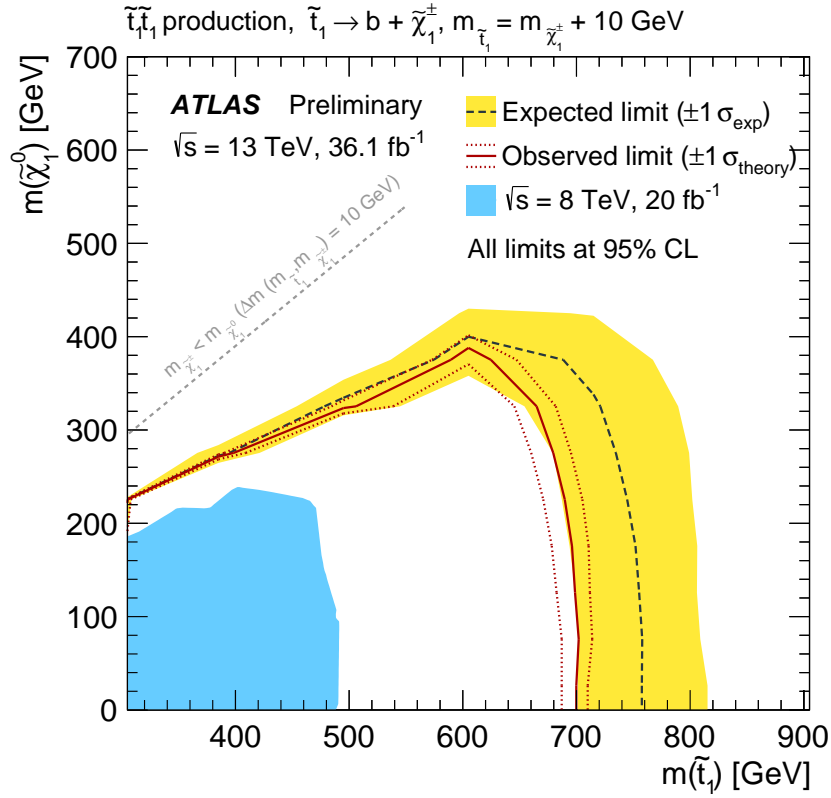
Figure 9: Exclusion contour for a simplified model assuming $\tilde{t}_1$ pair production, decaying via $\tilde{t}_1 \rightarrow b\tilde{\chi}_1^\pm$ with 100% branching ratio. The lightest chargino mass is assumed to be close to the stop mass, $m_{\tilde{\chi}_1^\pm} = m_{\tilde{t}_1} - 10$ GeV. The dashed grey line and the shaded band are the expected limit and its $\pm 1\sigma$ uncertainty. The thick solid red line is the observed limit for the central value of the signal cross-section. The expected and observed limits do not include the effect of the theoretical uncertainties on the signal cross-section. The dotted lines show the effect on the observed limit when varying the signal cross-section by $\pm 1\sigma$ of the theoretical uncertainty. The shaded blue area shows the observed exclusion from the ATLAS $\sqrt{s} = 8$ TeV analysis [22].
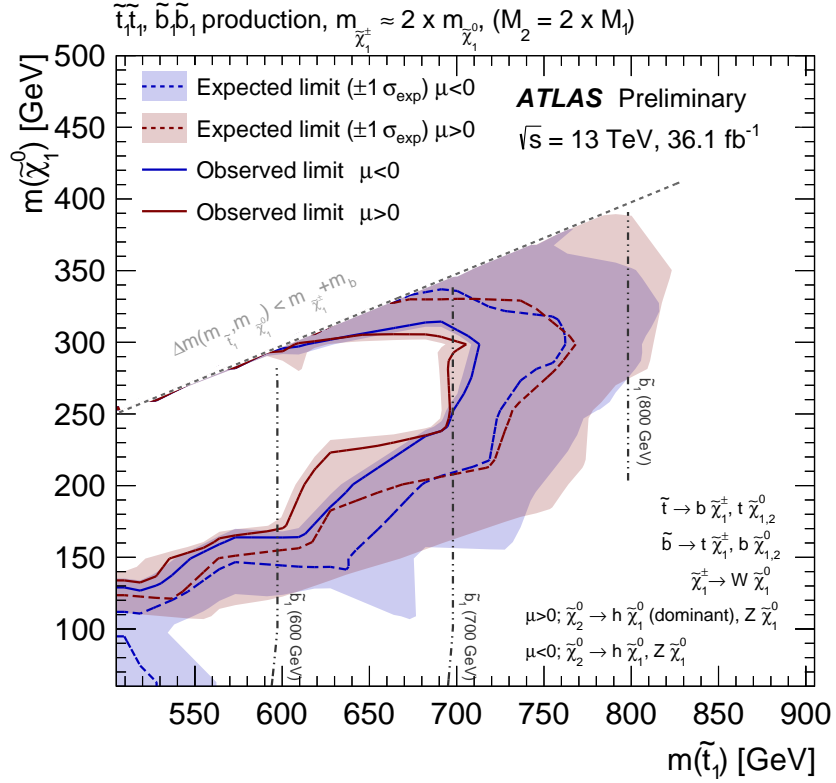
Figure 10: Exclusion contour as a function of $m_{\tilde{t}_1}$ and $m_{\tilde{\chi}_1^0}$ in the pMSSM model described in the text. Pair production of $\tilde{t}_1$ and $\tilde{b}_1$ are considered. Limits are set for both positive (red in the figure) and negative (blue in the figure) values of μ. The dashed and dotted grey lines indicate constant values of the $\tilde{b}_1$ mass. The signal models included within the shown contours are excluded at 95% CL. The dashed lines and the shaded band are the expected limit and its $\pm 1\sigma$ uncertainty. The thick solid line is the observed limit for the central value of the signal cross-section. The expected and observed limits do not include the effect of the theoretical uncertainties on the signal cross-section.

9 Conclusion

This article reports a search for top squark pair production in final states containing two leptons and large missing transverse momentum, based on a 36.1 fb^{-1}dataset of $\sqrt{s} = 13$ TeV proton-proton collisions recorded by the ATLAS experiment at the LHC in 2015 and 2016. Good agreement has been found between the observed events in the data and the expected Standard Model yields.

Model-independent 95% CL upper limits on the visible cross-section for new phenomena have been computed. The results are also interpreted in terms of simplified models assuming a range of top squark and lightest neutralino masses, with the former decaying to the latter via either a direct two-, three- or four-body decay or via an intermediate chargino state. In the case of top squark decays to $t^{(*)}\tilde{\chi}_1^0$, top squark masses below 720 GeV are excluded for a massless lightest neutralino. In the three-body decay hypothesis, top squark masses are excluded up to 430 GeV for $m_{\tilde{t}_1} - m_{\tilde{\chi}_1^0}$ close to the W boson mass. In the four-body decay hypothesis, top squark masses are excluded up to 400 GeV for $m_{\tilde{t}_1} - m_{\tilde{\chi}_1^0} = 40$ GeV. Both these results extend the coverage of previous searches by about 100 GeV. The chargino decay mode, $\tilde{t}_1 \to b\tilde{\chi}_1^\pm$, is excluded for top squark masses up to 700 GeV, assuming that $m_{\tilde{t}_1} - m_{\tilde{\chi}_1^\pm} = 10$ GeV, extending the previous results by almost 200 GeV. When considering a pMSSM inspired model including multiple decay chains, top squark masses up to about 700 GeV are excluded for a lightest neutralino of about 280 GeV. These results extend the region of supersymmetric parameter space excluded by previous LHC searches.

References

[1] F. Zwicky, *Die Rotverschiebung von extragalaktischen Nebeln*, Helv. Phys. Acta **6** (1933) 110.

[2] G. Bertone, D. Hooper and J. Silk, *Particle dark matter: evidence, candidates and constraints*, Phys. Rept. **405** (2005) 279, arXiv: `hep-ph/0404175`.

[3] G. Jungman, M. Kamionkowski and K. Griest, *Supersymmetric dark matter*, Phys. Rept. **267** (1996) 195, arXiv: `hep-ph/9506380 [hep-ph]`.

[4] J. Binney and S. Tremaine, *Galactic Dynamics*, Second, Princeton Series in Astrophysics, Princeton University Press, 2008.

[5] Y. Golfand and E. Likhtman, *Extension of the Algebra of Poincare Group Generators and Violation of p Invariance*, JETP Lett. **13** (1971) 323.

[6] D. Volkov and V. Akulov, *Is the Neutrino a Goldstone Particle?*, Phys. Lett. B **46** (1973) 109.

[7] J. Wess and B. Zumino, *Supergauge Transformations in Four-Dimensions*, Nucl. Phys. B **70** (1974) 39.

[8] J. Wess and B. Zumino, *Supergauge Invariant Extension of Quantum Electrodynamics*, Nucl. Phys. B **78** (1974) 1.

[9] S. Ferrara and B. Zumino, *Supergauge Invariant Yang-Mills Theories*, Nucl. Phys. B **79** (1974) 413.

[10] A. Salam and J. A. Strathdee, *Supersymmetry and Nonabelian Gauges*, Phys. Lett. B **51** (1974) 353.

[11] C. Regis et al., *Search for Proton Decay via $p \rightarrow \mu^+ K^0$ in Super-Kamiokande I, II, and III*, Phys. Rev. D **86** (2012) 012006, arXiv: `1205.6538 [hep-ex]`.

[12] G. R. Farrar and P. Fayet, *Phenomenology of the Production, Decay, and Detection of New Hadronic States Associated with Supersymmetry*, Phys. Lett. B **76** (1978) 575.

[13] P. Fayet, *Supersymmetry and Weak, Electromagnetic and Strong Interactions*, Phys. Lett. B **64** (1976) 159.

[14] P. Fayet, *Spontaneously Broken Supersymmetric Theories of Weak, Electromagnetic and Strong Interactions*, Phys. Lett. B **69** (1977) 489.

[15] H. Goldberg, *Constraint on the Photino Mass from Cosmology*, Phys. Rev. Lett. **50** (1983) 1419, [Erratum: Phys. Rev. Lett.103,099905(2009)].

[16] J. R. Ellis et al., *Supersymmetric Relics from the Big Bang*, Nucl. Phys. B **238** (1984) 453.

[17] J. Alwall et al., *Searching for Directly Decaying Gluinos at the Tevatron*, Phys. Lett. B **666** (2008) 34, arXiv: `0803.0019 [hep-ph]`.

[18] J. Alwall, P. Schuster and N. Toro,
Simplified Models for a First Characterization of New Physics at the LHC,
Phys. Rev. D **79** (2009) 075020, arXiv: 0810.3921 [hep-ph].

[19] D. Alves, *Simplified Models for LHC New Physics Searches*,
J. Phys. G **39** (2012) 105005, ed. by N. Arkani-Hamed et al., arXiv: 1105.2838 [hep-ph].

[20] A. Djouadi et al., 'The Minimal supersymmetric standard model: Group summary report',
GDR (Groupement De Recherche) - Supersymetrie Montpellier, France, April 15-17, 1998, 1998,
arXiv: hep-ph/9901246 [hep-ph],
URL: https://inspirehep.net/record/481987/files/arXiv:hep-ph_9901246.pdf.

[21] C. F. Berger et al., *Supersymmetry without prejudice*, JHEP **02** (2009) 023,
arXiv: 0812.0980 [hep-ph].

[22] ATLAS Collaboration, *ATLAS Run 1 searches for direct pair production of third-generation
squarks at the Large Hadron Collider*, Eur. Phys. J. C **75** (2015) 510,
arXiv: 1506.08616 [hep-ex].

[23] ATLAS Collaboration, *Search for top squarks in final states with one isolated lepton, jets, and
missing transverse momentum in $\sqrt{s}$ = 13 TeV pp collisions with the ATLAS detector*,
Phys. Rev. D **94** (2016) 052009, arXiv: 1606.03903 [hep-ex].

[24] CMS Collaboration, *Search for top-squark pair production in the single-lepton final state in pp
collisions at $\sqrt{s}$ = 8 TeV*, Eur. Phys. J. C **73** (2013) 2677, arXiv: 1308.1586 [hep-ex].

[25] CMS Collaboration, *Search for supersymmetry using razor variables in events with b-tagged jets
in pp collisions at $\sqrt{s}$ = 8 TeV*, Phys. Rev. D **91** (2015) 052018, arXiv: 1502.00300 [hep-ex].

[26] CMS Collaboration, *Searches for supersymmetry using the M_{T2} variable in hadronic events
produced in pp collisions at 8 TeV*, JHEP **05** (2015) 078, arXiv: 1502.04358 [hep-ex].

[27] CMS Collaboration, *Search for direct pair production of supersymmetric top quarks decaying to
all-hadronic final states in pp collisions at $\sqrt{s}$ = 8 TeV*, Eur. Phys. J. C **76** (2016) 460,
arXiv: 1603.00765 [hep-ex].

[28] CMS Collaboration, *Searches for third-generation squark production in fully hadronic final
states in proton–proton collisions at $\sqrt{s}$ = 8 TeV*, JHEP **06** (2015) 116,
arXiv: 1503.08037 [hep-ex].

[29] CMS Collaboration, *Search for top squark pair production in compressed-mass-spectrum
scenarios in proton–proton collisions at $\sqrt{s}$ = 8 TeV using the α_{T} variable*,
Phys. Lett. **B767** (2017) 403, arXiv: 1605.08993 [hep-ex].

[30] CMS Collaboration, *Search for direct pair production of scalar top quarks in the single- and
dilepton channels in proton–proton collisions at $\sqrt{s}$ = 8 TeV*, JHEP **07** (2016) 027,
arXiv: 1602.03169 [hep-ex].

[31] CMS Collaboration, *Search for supersymmetry in events with soft leptons, low jet multiplicity,
and missing transverse energy in proton–proton collisions at $\sqrt{s}$ = 8 TeV*,
Phys. Lett. B **759** (2016) 9, arXiv: 1512.08002 [hep-ex].

[32] CMS Collaboration, *Search for new physics with the M_{T2} variable in all-jets final states produced in pp collisions at $\sqrt{s}$ = 13 TeV*, JHEP **10** (2016) 006, arXiv: 1603.04053 [hep-ex].

[33] CMS Collaboration, *Inclusive search for supersymmetry using razor variables in pp collisions at $\sqrt{s}$ = 13 TeV*, Phys. Rev. **D95** (2016) 012003, arXiv: 1609.07658 [hep-ex].

[34] CMS Collaboration, *A search for new phenomena in pp collisions at $\sqrt{s}$ = 13 TeV in final states with missing transverse momentum and at least one jet using the α_T variable*, Eur. Phys. J. C (2016), arXiv: 1611.00338 [hep-ex].

[35] CMS Collaboration, *Searches for pair production for third-generation squarks in sqrt(s)=13 TeV pp collisions*, (2016), arXiv: 1612.03877 [hep-ex].

[36] CMS Collaboration, *Search for supersymmetry in the all-hadronic final state using top quark tagging in pp collisions at $\sqrt{s}$ = 13 TeV*, (2017), arXiv: 1701.01954 [hep-ex].

[37] ATLAS Collaboration, *The ATLAS Experiment at the CERN Large Hadron Collider*, JINST **3** (2008) S08003.

[38] ATLAS Collaboration, *ATLAS Insertable B-Layer Technical Design Report*, 2010, URL: https://cds.cern.ch/record/1291633.

[39] ATLAS Collaboration, *Luminosity determination in pp collisions at $\sqrt{s}$ = 8 TeV using the ATLAS detector at the LHC*, Eur. Phys. J. **C76** (2016) 653, arXiv: 1608.03953 [hep-ex].

[40] *Electron efficiency measurements with the ATLAS detector using 2012 LHC proton-proton collision data*, Eur. Phys. J. **C77** (2017) 195, arXiv: 1612.01456 [hep-ex].

[41] ATLAS Collaboration, *Muon reconstruction performance of the ATLAS detector in proton–proton collision data at $\sqrt{s}$ = 13 TeV*, Eur. Phys. J. C **76** (2016) 292, arXiv: 1603.05598 [hep-ex].

[42] ATLAS Collaboration, *Topological cell clustering in the ATLAS calorimeters and its performance in LHC Run 1*, (2016), arXiv: 1603.02934 [hep-ex].

[43] M. Cacciari, G. P. Salam and G. Soyez, *The anti-k_t jet clustering algorithm*, JHEP **04** (2008) 063, arXiv: 0802.1189 [hep-ph].

[44] ATLAS Collaboration, *A measurement of the calorimeter response to single hadrons and determination of the jet energy scale uncertainty using LHC Run-1 pp-collision data with the ATLAS detector*, Eur. Phys. J. **C77** (2017) 26, arXiv: 1607.08842 [hep-ex].

[45] ATLAS Collaboration, *Jet energy scale measurements and their systematic uncertainties in proton-proton collisions at sqrt(s) = 13 TeV with the ATLAS detector*, (2017), arXiv: 1703.09665 [hep-ex].

43

[46] ATLAS Collaboration, *Jet Calibration and Systematic Uncertainties for Jets Reconstructed in the ATLAS Detector at $\sqrt{s}$ = 13 TeV*, ATL-PHYS-PUB-2015-015, 2015, URL: https://cds.cern.ch/record/2037613.

[47] ATLAS Collaboration, *Tagging and suppression of pileup jets with the ATLAS detector*, ATLAS-CONF-2014-018, 2014, URL: https://cds.cern.ch/record/1700870.

[48] ATLAS Collaboration, *Optimization of the ATLAS b-tagging performance for the 2016 LHC Run*, ATL-PHYS-PUB-2016-012, 2016, URL: http://cds.cern.ch/record/2160731.

[49] ATLAS Collaboration, *Performance of b-jet identification in the ATLAS experiment*, JINST **11** (2016) P04008, arXiv: 1512.01094 [hep-ex].

[50] ATLAS Collaboration, *Data-Quality Requirements and Event Cleaning for Jets and Missing Transverse Energy Reconstruction with the ATLAS Detector in Proton–Proton Collisions at a Center-of-Mass Energy of $\sqrt{s}$ = 7 TeV*, ATLAS-CONF-2010-038, 2010, URL: https://cds.cern.ch/record/1277678.

[51] ATLAS Collaboration, *Performance of missing transverse momentum reconstruction for the ATLAS detector in the first proton-proton collisions at at $\sqrt{s}$= 13 TeV*, ATL-PHYS-PUB-2015-027, 2015, URL: http://cds.cern.ch/record/2037904.

[52] ATLAS Collaboration, *Expected performance of missing transverse momentum reconstruction for the ATLAS detector at $\sqrt{s}$ = 13 TeV*, ATL-PHYS-PUB-2015-023, 2015, URL: http://cds.cern.ch/record/2037700.

[53] T. Melia, *Spin before mass at the LHC*, JHEP **01** (2012) 143, arXiv: 1110.6185 [hep-ph].

[54] C. G. Lester and D. J. Summers, *Measuring masses of semiinvisibly decaying particles pair produced at hadron colliders*, Phys. Lett. B **463** (1999) 99, arXiv: hep-ph/9906349.

[55] A. Barr, C. Lester and P. Stephens, *A variable for measuring masses at hadron colliders when missing energy is expected; m_{T2}: The Truth behind the glamour*, J. Phys. **G29** (2003) 2343, arXiv: hep-ph/0304226 [hep-ph].

[56] W. S. Cho et al., *Measuring superparticle masses at hadron collider using the transverse mass kink*, JHEP **02** (2008) 035, arXiv: 0711.4526 [hep-ph].

[57] M. Burns et al., *Using subsystem M_{T2} for complete mass determinations in decay chains with missing energy at hadron colliders*, JHEP **03** (2009) 143, arXiv: 0810.5576 [hep-ph].

[58] M. R. Buckley et al., *Super-razor and searches for sleptons and charginos at the LHC*, Phys. Rev. D **89** (2014) 055020, arXiv: 1310.4827 [hep-ph].

[59] ATLAS Collaboration, *Simulation of top quark production for the ATLAS experiment at $\sqrt{s}$ = 13 TeV*, ATL-PHYS-PUB-2016-004, 2016, URL: https://cds.cern.ch/record/2120417.

[60] ATLAS Collaboration, *Monte Carlo Generators for the Production of a W or Z/γ* Boson in Association with Jets at ATLAS in Run 2*, ATL-PHYS-PUB-2016-003, 2016, URL: https://cds.cern.ch/record/2120133.

[61] ATLAS Collaboration, *Multi-Boson Simulation for 13 TeV ATLAS Analyses*, ATL-PHYS-PUB-2016-002, 2016, URL: https://cds.cern.ch/record/2119986.

[62] ATLAS Collaboration, *Modelling of the $t\bar{t}H$ and $t\bar{t}V$ ($V = W, Z$) processes for $\sqrt{s}$ = 13 TeV ATLAS analyses*, ATL-PHYS-PUB-2016-005, 2016, URL: https://cds.cern.ch/record/2120826.

[63] D. J. Lange, *The EvtGen particle decay simulation package*, Nucl. Instrum. Meth. A **462** (2001) 152.

[64] J. Alwall et al., *The automated computation of tree-level and next-to-leading order differential cross sections, and their matching to parton shower simulations*, JHEP **07** (2014) 079, arXiv: 1405.0301 [hep-ph].

[65] T. Sjöstrand, S. Mrenna and P. Z. Skands, *A brief introduction to PYTHIA 8.1*, Comput. Phys. Commun. **178** (2008) 852, arXiv: 0710.3820 [hep-ph].

[66] W. Beenakker et al., *Squark and gluino production at hadron colliders*, Nucl.Phys.B **492** (1997) 51, arXiv: hep-ph/9610490 [hep-ph].

[67] A. Kulesza and L. Motyka, *Threshold resummation for squark-antisquark and gluino-pair production at the LHC*, Phys.Rev.Lett. **102** (2009) 111802, arXiv: 0807.2405 [hep-ph].

[68] A. Kulesza and L. Motyka, *Soft gluon resummation for the production of gluino-gluino and squark-antisquark pairs at the LHC*, Phys.Rev. **D80** (2009) 095004, arXiv: 0905.4749 [hep-ph].

[69] W. Beenakker et al., *Soft-gluon resummation for squark and gluino hadroproduction*, JHEP **12** (2009) 041, arXiv: 0909.4418 [hep-ph].

[70] W. Beenakker et al., *Squark and Gluino Hadroproduction*, Int. J. Mod. Phys. **A26** (2011) 2637, arXiv: 1105.1110 [hep-ph].

[71] C. Borschensky et al., *Squark and gluino production cross sections in pp collisions at $\sqrt{s}$ = 13, 14, 33 and 100 TeV*, Eur.Phys.J. **C74** (2014) 3174, arXiv: 1407.5066 [hep-ph].

[72] H.-L. Lai et al., *New parton distributions for collider physics*, Phys. Rev. **D82** (2010) 074024, arXiv: 1007.2241 [hep-ph].

[73] ATLAS Collaboration, *ATLAS Pythia8 tunes to 7 TeV data*, ATL-PHYS-PUB-2014-021, 2014, URL: http://cds.cern.ch/record/1966419.

[74] T. Gleisberg et al., *Event generation with SHERPA 1.1*, JHEP **02** (2009) 007, arXiv: 0811.4622 [hep-ph].

[75] S. Catani et al.,
Vector boson production at hadron colliders: a fully exclusive QCD calculation at NNLO,
Phys. Rev. Lett. **103** (2009) 082001, arXiv: `0903.2120 [hep-ph]`.

[76] S. Alioli et al., *A general framework for implementing NLO calculations in shower Monte Carlo programs: the POWHEG BOX*, JHEP **06** (2010) 043, arXiv: `1002.2581 [hep-ph]`.

[77] T. Sjöstrand, S. Mrenna and P. Z. Skands, *PYTHIA 6.4 Physics and Manual*,
JHEP **0605** (2006) 026, arXiv: `hep-ph/0603175 [hep-ph]`.

[78] M. Czakon, P. Fiedler and A. Mitov,
Total Top-Quark Pair-Production Cross Section at Hadron Colliders Through $O(\alpha_S^4)$,
Phys. Rev. Lett. **110** (2013) 252004, arXiv: `1303.6254 [hep-ph]`.

[79] M. Czakon and A. Mitov,
NNLO corrections to top pair production at hadron colliders: the quark-gluon reaction,
JHEP **1301** (2013) 080, arXiv: `1210.6832 [hep-ph]`.

[80] M. Czakon and A. Mitov, *NNLO corrections to top-pair production at hadron colliders: the all-fermionic scattering channels*, JHEP **1212** (2012) 054, arXiv: `1207.0236 [hep-ph]`.

[81] P. Bärnreuther, M. Czakon and A. Mitov, *Percent Level Precision Physics at the Tevatron: First Genuine NNLO QCD Corrections to $q\bar{q} \rightarrow t\bar{t} + X$*, Phys. Rev. Lett. **109** (2012) 132001,
arXiv: `1204.5201 [hep-ph]`.

[82] M. Cacciari et al., *Top-pair production at hadron colliders with next-to-next-to-leading logarithmic soft-gluon resummation*, Phys. Lett. B **710** (2012) 612,
arXiv: `1111.5869 [hep-ph]`.

[83] M. Czakon and A. Mitov,
Top++: a program for the calculation of the top-pair cross-section at hadron colliders,
Comput.Phys.Commun. **185** (2014) 2930, arXiv: `1112.5675 [hep-ph]`.

[84] P. Z. Skands, *Tuning Monte Carlo generators: the Perugia tunes*, Phys.Rev. **D82** (2010) 074018,
arXiv: `1005.3457 [hep-ph]`.

[85] N. Kidonakis,
Two-loop soft anomalous dimensions for single top quark associated production with a W- or H-,
Phys.Rev. **D 82** (2010) 054018, arXiv: `1005.4451 [hep-ph]`.

[86] G. Corcella et al., *HERWIG 6: An Event generator for hadron emission reactions with interfering gluons (including supersymmetric processes)*, JHEP **01** (2001) 010,
arXiv: `hep-ph/0011363 [hep-ph]`.

[87] LHC Higgs Cross Section Working Group,
Handbook of LHC Higgs Cross Sections: 2. Differential Distributions,
CERN-2012-002 (CERN, Geneva, 2012), arXiv: `1201.3084 [hep-ph]`.

[88] P. Artoisenet et al.,
Automatic spin-entangled decays of heavy resonances in Monte Carlo simulations,
JHEP **03** (2013) 015, arXiv: `1212.3460 [hep-ph]`.

[89] L. Lönnblad and S. Prestel, *Matching tree-level matrix elements with interleaved showers*, JHEP **03** (2012) 019, arXiv: `1109.4829 [hep-ph]`.

[90] W. Beenakker et al., *Stop production at hadron colliders*, Nucl. Phys. **B515** (1998) 3, arXiv: `hep-ph/9710451 [hep-ph]`.

[91] W. Beenakker et al., *Supersymmetric top and bottom squark production at hadron colliders*, JHEP **08** (2010) 098, arXiv: `1006.4771 [hep-ph]`.

[92] B. C. Allanach, *SOFTSUSY: a program for calculating supersymmetric spectra*, Comput. Phys. Commun. **143** (2002) 305, arXiv: `hep-ph/0104145 [hep-ph]`.

[93] W. Porod, *SPheno, a program for calculating supersymmetric spectra, SUSY particle decays and SUSY particle production at e+ e- colliders*, Comput. Phys. Commun. **153** (2003) 275, arXiv: `hep-ph/0301101 [hep-ph]`.

[94] W. Porod and F. Staub, *SPheno 3.1: Extensions including flavour, CP-phases and models beyond the MSSM*, Comput. Phys. Commun. **183** (2012) 2458, arXiv: `1104.1573 [hep-ph]`.

[95] A. Djouadi, J.-L. Kneur and G. Moultaka, *SuSpect: A Fortran code for the supersymmetric and Higgs particle spectrum in the MSSM*, Comput. Phys. Commun. **176** (2007) 426, arXiv: `hep-ph/0211331 [hep-ph]`.

[96] A. Djouadi, M. M. Muhlleitner and M. Spira, *Decays of supersymmetric particles: The Program SUSY-HIT (SUspect-SdecaY-Hdecay-InTerface)*, Acta Phys. Polon. **B38** (2007) 635, arXiv: `hep-ph/0609292 [hep-ph]`.

[97] ATLAS Collaboration, *Summary of ATLAS Pythia 8 tunes*, ATLAS-PHYS-PUB-2012-003, 2012, URL: `http://cdsweb.cern.ch/record/1474107`.

[98] A. D. Martin et al., *Parton distributions for the LHC*, Eur. Phys. J. **C63** (2009) 189, arXiv: `0901.0002 [hep-ph]`.

[99] ATLAS Collaboration, *The ATLAS Simulation Infrastructure*, Eur.Phys.J. **C70** (2010) 823, arXiv: `1005.4568 [physics.ins-det]`.

[100] S. Agostinelli et al., *GEANT4: a simulation toolkit*, Nucl.Instrum.Meth.A **506** (2003) 250.

[101] ATLAS Collaboration, *The simulation principle and performance of the ATLAS fast calorimeter simulation FastCaloSim*, ATL-PHYS-PUB-2010-013, 2010, URL: `http://cds.cern.ch/record/1300517`.

[102] M. Baak et al., *HistFitter software framework for statistical data analysis*, Eur. Phys. J. C **75** (2015) 153, arXiv: `1410.1280 [hep-ex]`.

[103] ATLAS collaboration, *Measurement of the top quark-pair production cross section with ATLAS in pp collisions at $\sqrt{s}$ = 7 TeV*, Eur. Phys. J. C **71** (2011) 1577, arXiv: `1012.1792 [hep-ex]`.

[104] ATLAS collaboration, *Measurement of the top quark pair production cross section in pp collisions at $\sqrt{s}$ = 7 TeV in dilepton final states with ATLAS*, Phys. Lett. B **707** (2012) 459, arXiv: `1108.3699 [hep-ex]`.

[105] ATLAS Collaboration, *Calibration of b-tagging using dileptonic top pair events in a combinatorial likelihood approach with the ATLAS experiment*, ATLAS-CONF-2014-004, 2014, URL: https://cds.cern.ch/record/1664335.

[106] ATLAS Collaboration, *Calibration of the performance of b-tagging for c and light-flavour jets in the 2012 ATLAS data*, ATLAS-CONF-2014-046, 2014, URL: https://cds.cern.ch/record/1741020.

[107] ATLAS Collaboration, *Multi-Boson Simulation for 13 TeV ATLAS Analyses*, ATL-PHYS-PUB-2016-002, 2016, URL: http://cds.cern.ch/record/2119986.

[108] ATLAS Collaboration, *Modelling of the $t\bar{t}H$ and $t\bar{t}V$ ($V = W, Z$) processes for $\sqrt{s}$ = 13 TeV ATLAS analyses*, ATL-PHYS-PUB-2015-022, 2016, URL: http://cds.cern.ch/record/2120826.

[109] P. Kant et al., *HatHor for single top-quark production: Updated predictions and uncertainty estimates for single top-quark production in hadronic collisions*, Comput. Phys. Commun. **191** (2015) 74, arXiv: 1406.4403 [hep-ph].

[110] A. L. Read, *Presentation of search results: The CL_s technique*, J. Phys. G **28** (2002) 2693.
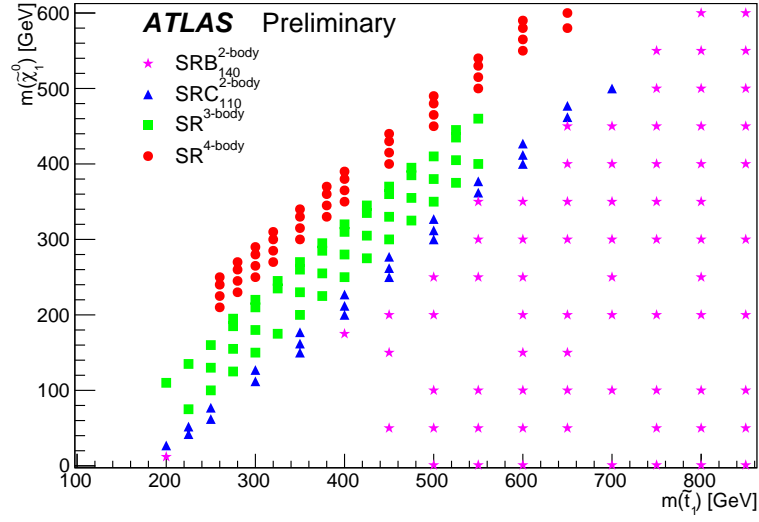
Appendix

Figure 11: Illustration of the best expected signal region per signal grid point for the simplified model assuming $\tilde{t}_1$ pair production, decaying via $\tilde{t}_1 \rightarrow t^{(*)} \tilde{\chi}_1^0$ with 100% branching ratio.